Using numerical analysis to design and optimize river hydrokinetic turbine to address seasonal velocity variations

by

Bahador Shaabani

A Thesis Submitted to the Faculty of Graduate Studies of
the University of Manitoba
in Partial Fulfilment of the Requirements of the Degree of

MASTER OF SCIENCE

Department of Mechanical Engineering
The University of Manitoba
Winnipeg

Abstract

Seasonal velocity variations can significantly impact total energy delivered to microgrids produced by river hydrokinetic turbines. These turbines typically use a diffuser to increase the velocity at the rotor section, adding weight and increasing deployment and retrieval costs. There is a need for practical solutions to improve the capacity factor of such turbines for remote communities. Part of the solution is addressed by developing multiple turbine rotors that can be interchanged to match seasonal velocity variations and thereby eliminate the need for shrouds to simplify the design and reduce costs. The proposed approach employs different rotor sizes to address seasonal river velocity changes, modifying the turbine power curve to increase the yearly river turbine capacity factor. A turbine design that can be surfaced using boats available in remote communities is used to allow 2 blades rotor changes. BladeGen ANSYS Workbench is used to design the three rotors of decreasing size for free stream velocities of 1.6, 2.2, and 2.8 m/s. For each hydrokinetic turbine rotor, the 3D simulation is applied to reduce aerodynamic losses and target a coefficient of performance of up to 45%, by optimizing the blade shape and rotor aerodynamic parameters. Mechanical stress analyses determine the maximum displacement and blade stress for stainless steel and composite materials. Numerical results were compared to experimental results: the pressure coefficient against the tip speed ratio demonstrated good agreement with the experimental data. Based on the simulations, the three rotor efficiencies varied from 43% to 45% at a TSR of 4, the point at which the maximum pressure coefficient was observed in numerical and experimental results, while the power output varied from 5.4 to 5.6 kW for the three velocities investigated. Results show that it is possible to significantly increase turbine capacity factors by interchanging rotors to account for seasonal velocity variations in rivers.

Acknowledgements

I am grateful to my supervisor, Dr. Vijay Chatoorgoon, for allowing me to finish my thesis. I express my sincere gratitude for his valuable support and encouragement. I would also like to express my deepest appreciation to Dr. Eric Bibeau for his valuable advice and support. His guidance and patience have been invaluable in the development of my work. I would also like to thank Dr. Jinxing Huang from NRCAN for his time and invaluable assistance and guidance. Finally, and on a personal level, I want to express my appreciation to my mother, Parvin, and my brother, Behnam. It would not have been possible for me to complete the project without their support and encouragement.

Contents

List of Tables

List of Figures

Abbreviations

3-D	Three-Dimensional
BEMT	Blade Element Momentum Theory
CFD	Computational Fluid Dynamics
Cp	Pressure Coefficient
DER	Distributed Energy Resources
GGI	Generalized Grid Interface
HATT	Horizontal Axis Tidal Turbine
HAHT	Horizontal Axis Hydrokinetic Turbine
NACA	National Advisory Committee for Aeronautics
RANS	Reynolds-Averaged Navier-Stokes
RE	Renewable Energy
RHKT	River hydrokinetic turbines
Rsh	Shroud Radius
SST	Shear Stress Turbulence

1. Introduction

1.1. Renewable energy

Economic growth is significantly influenced by energy. However, the overconsumption of fossil fuels contributes to the depletion of natural energy resources and has negative environmental consequences. Therefore, it is necessary to investigate and prioritize renewable energy that is more sustainable to ensure long-term economic growth and environmental sustainability.

There has been a remarkable and concerning increase in CO_2 levels in recent years. This increase has far-reaching impacts on the climate, ecosystems, and biodiversity. According to the Global Carbon Project, the concentration of CO_2 in the atmosphere increased by 49% from 1750 to 2020, reaching a level of 414 parts per million. To mitigate the adverse effects of increasing CO_2 levels and combat climate change, it is necessary to reduce CO_2 emissions significantly. It is estimated that 1.4 billion tons of CO_2 emissions need to be reduced annually to achieve net zero emissions by 2050. However, CO_2 level was 418 ppm in November 2022, and is expected to reach 800 parts per million by 2100[1]. This increase in CO_2 concentrations is projected to lead to a corresponding increase in global temperatures, with an estimated rise of 4.5 degrees Celsius. These rising CO_2 levels and temperatures will significantly impact the planet, including changes to ecosystems and species and exacerbating natural disasters.

Renewable energy contributes to the optimization of energy infrastructure, the balance of supply and demand, and the protection of the environment. It is imperative that renewable energy accounts for at least two-thirds of energy consumption worldwide and contribute to greenhouse gas emissions reductions required by the end of 2050 to hold the global average surface temperature rise below two degrees Celsius[2].

The international community has recognized the need to take action to address the issue of climate change. This goal can be achieved by having fifty percent of known fossil fuel reserves unused, and fifty percent of the energy must be derived from renewable sources [3]. Moreover, to achieve sustainable development, energy needs to be affordable, dependable, sustainable, and modern. As stated in the sustainable development goals, ensuring everyone has access to electricity is essential[4].

In recent decades, renewable energy sources have been developed to meet the energy needs of remote areas that do not have access to electrical grids[5]. The most common types of renewable energy are hydropower, biomass, solar photovoltaic, and wind power resources.

It is estimated that there are approximately 239 communities spread across Canada's vast northern regions. These communities must deal with constant issues relating to energy availability and the environment. Delivering fuel to isolated communities has resulted in significant environmental and economic consequences. For communities with only road transportation through winter, warming costs are increased particularly during winter. Because of old storage facilities, more than 1,440 sites on First Nations reserves are contaminated. The cleanup is expected to cost CAD 458 million[6]. Figure 1 shows the community with diesel power in Canada.

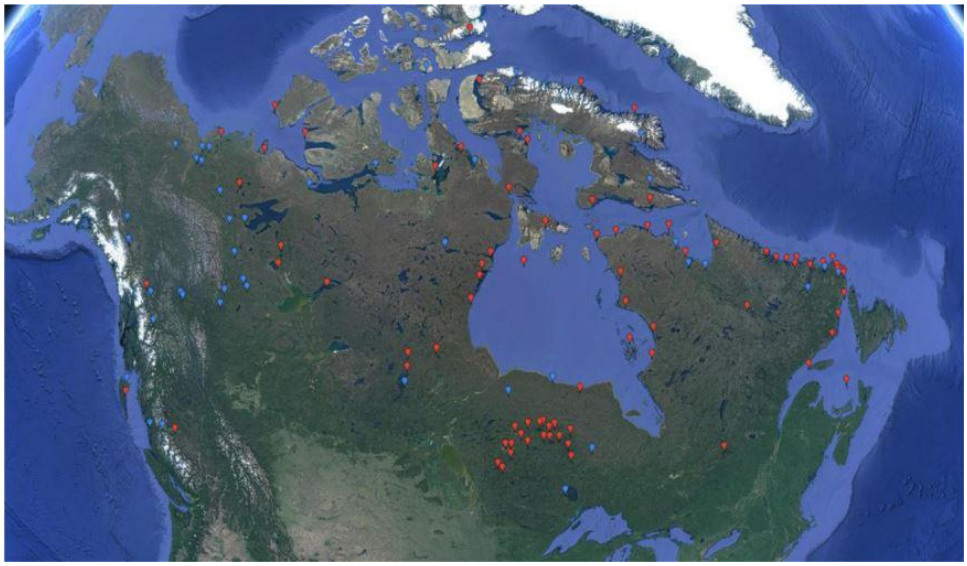

Figure 1: Canadian communities with diesel power from NRCAN

Microgrids have been developed as an application of renewable energy resources. The term microgrid refers to a distribution-level grid that contains multiple renewable energy systems with storage. As opposed to conventional power plants, microgrids can be more environmentally friendly because they reduce transmission power losses, eliminate traffic congestion, and can improve power system reliability[7]. For instance, two types of optimal microgrid planning are shown in Figure 2. As shown, a microgrid system consists of batteries, converters, diesel generators, solar panels, wind power, and hydropower sources. All these components can be employed in a microgrid, or one or more of them can be eliminated from the grid for remote areas, depending on capacity and ability. Consequently, several unique options can be considered for microgrids, including hydrokinetic energy resources.

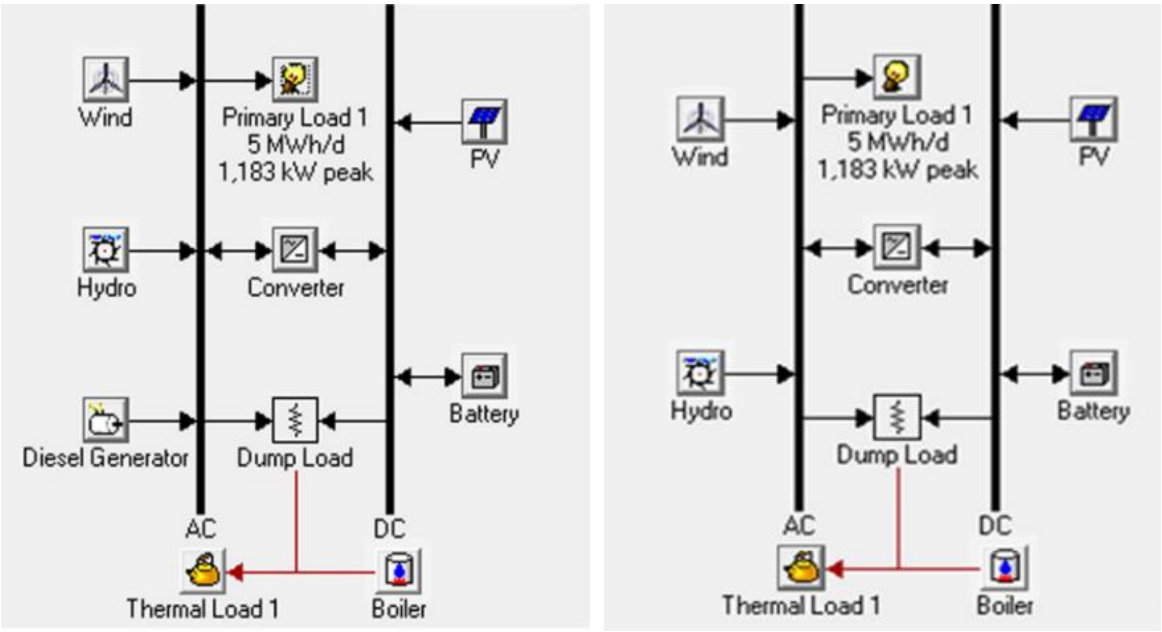

Figure 2: Various optimal microgrid planning [8]

1.2. Hydrokinetic energy

The process of producing energy from water is known as hydropower. Water sources generate electricity by converting their gravitational potential or kinetic energy into electricity. Hydropower is widely recognized as the world's most significant renewable source for installed capacity. Due to its regularity and availability, hydropower is one of the most usable options for producing energy. Traditionally, hydropower has been developed using static hard. To create a pressure head, water is retained in reservoirs. Then the turbine is used to extract energy from the water.

River hydrokinetic turbines (RHKT) use water flow velocities between 1 to 4 m/s to produce power. RHKT offers a viable and potential solution for generating electricity in remote applications in micro-grid arrangement. These systems do not require dam construction, making them flexible and adaptable to multiple locations. RHKT systems make them particularly suitable for use in developing countries, where they can provide

electricity to remote communities that may not have access to other forms of power. Overall, the versatility and accessibility of RHKT systems could make them a valuable resource for meeting the energy needs of remote communities. Canada has a potential of 15 GW of river hydrokinetic power [9].

1.3. Hydrokinetic energy physics

RHKT operates on a similar principle to wind turbines. The difference between the two technologies is the fluid density through which the rotor is immersed. Water is roughly 850 times denser than air, so hydrokinetic systems can extract more energy per unit area[10]. Furthermore, RHKT operates in different flow regimes than traditional wind turbines and do not require a yawing unit.

To commercialize this technology, there is a significant obstacle in cost[11]. Another obstacle for RHKT is that at lower flow velocities, the power of the turbine system decreases due to the torque being related to the square of the flow velocity and power to the cube of the velocity. To enhance the power of low-speed, rotor torque must be increased, and resistive torque must be reduced. It is a challenging process to design turbines since the choice of design parameters directly impacts energy efficiency and cost-effectiveness. An optimal turbine design is necessary for practical application under various velocities. It is imperative that the blade design creates high lift forces. Among the necessary parameters for evaluating a RHKT performance is its rotor power coefficient, which impacts turbine efficiency[12]. In 1919 Betz's showed that a turbine's maximum efficiency is 59.3% [13]. To obtain maximum efficiency several elements are involved in the design of hydrofoils that must be optimized. The angle and topology of the various hydrofoils must be developed during the optimization process. It is also important to consider physical factors such as fluid velocity and attack angle [14]. However, capacity

factors can be low if seasonal flow velocities are much lower than the design speed of RHKT, negating any attempt to achieve high efficiency of the rotor. As mentioned, shroud complicated deployment. In addition, being able to deploy RHKT from shore further reduces costs.

It is proposed herein to address low-capacity factors of RHKT by changing the rotor size seasonally, eliminating the shroud, and use two-bladed rotors to allow to deploy the turbine close to the riverbank. These measures would reduce cost, increase micro-grid revenues, and reduce storage capacity requirement in micro-grids. Such RHKT would allow the end users to deploy them more quickly and easily, reducing installation time and maintenance costs.

Furthermore, it is possible to eliminate the need for gearbox with a hydraulic transmission using a hydraulic pump to drive each rotor. Power is transmitted to shore by a high-pressure hydraulic line, and a return line for low-pressure from shore to pump. There is a direct connection between an electric generator and one or more hydraulic motors onshore. There is a reduction in the cost of supporting structures[15]. As it is illustrated in Figure 3, instead of using one motor, multiple rotor-pump systems could increase output power. A simpler RHKT would allow interchange of the rotor more easily to account for seasonal velocity variations.

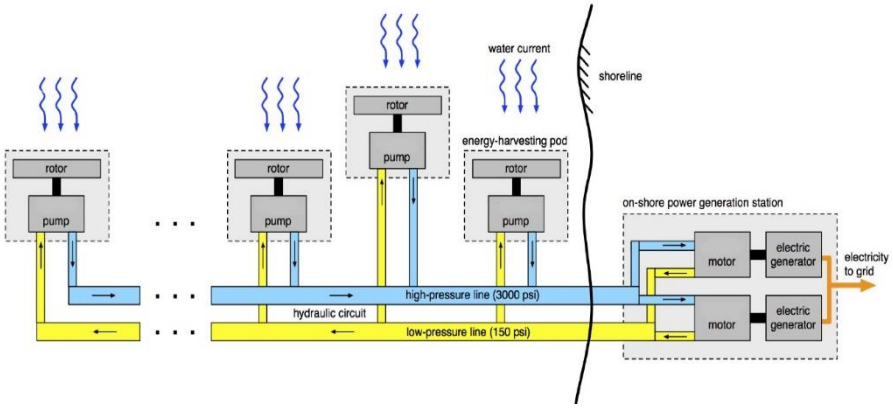

Figure 3: Block diagram of proposed method of hydrokinetic system

1.4. Design and optimization of rotor

In the field of rotor design, the blade design presents a significant challenge due to the complexity of the hydrofoil sections. These sections are characterized by variations in chord lines and twist angles distributed along the blade's length. Optimizing these geometric features, including the chord line, thickness, and twist angle requires advanced calculations and methodologies.

The complexity of these calculations arises from the interdependence of the parameters, which can affect the function of the blade, such as its lift and drag characteristics. As a result, finding the optimum values for these parameters is a multi-objective optimization problem that requires an iterative and systematic approach. Various mathematical methods and computational tools can be used to solve this problem, such as genetic algorithms, particle swarm optimization, and computational fluid dynamics simulations.

Additionally, the optimization process must consider the various constraints and requirements of the specific application, such as the operating conditions, material properties, and manufacturing limitations. Furthermore, optimization must also consider

the trade-offs between different performance objectives, such as maximizing lift while minimizing drag, or maximizing efficiency while minimizing weight.

In RHKT, the 3D optimization of multiple rotors for maximized power production is a challenging numerical problem with significant economic implications. It is complex and expensive to model turbines using computational fluid dynamics (CFD) because each rotor performance must be resolved as well as the flow field. Simulating these systems would take excessive time without using a High-Performance Computer (HPC). Reynolds-Averaged Navier Stokes (RANS) simulations are feasible for those with access to an HPC. However, the intricacy of such complicated models is not an insignificant barrier. To develop multiple rotors t that can be exchanged in the field to optimized efficiency and capacity factor requires to investigate the effectiveness of aerodynamic parameters and increases lift coefficient to obtain maximum efficiency using RANS solutions.

1.5. Research Objectives

The objective is to design changeable rotors to address seasonal velocity changes to increase the capacity factor of RHKT. Specifically,

i. designing and optimizing three rotors at three velocities ranges,
ii. using a numerical approach to analyze forces, pressure, velocity, and efficiency and optimize the aerodynamic parameters to achieve a target efficiency of over 40%, and
iii. investigating the mechanical behavior of the rotors for three different materials.

The insights and methodology developed in this research are meant to lead the way to develop a two-bladed turbine without a shroud, generating maximum power at low flow

rates.

1.6. Methodology

The methodology to achieve research objectives is:

- The BladeGen ANSYS Workbench software is employed to design three sizes of a two-blade horizontal axis river turbine.
- A 3-dimensional model is developed. ANSYS CFX performs the model preprocessing, imports the mesh, creates the domain, and sets up the physics, including turbulence, boundary conditions, interfaces, and results (power, torque). The ICEM CFD modeller and masher generate high-quality hexahedral grid domains for the upper and downstream and river channels. Simulations are conducted at the University of Manitoba on the Grex HPC.
- Static Structural Ansys Workbench is utilized for mechanical analysis. The blade geometry is imported from BladeGen and modified using Ansys design modeler. Pressure loading data is obtained from the CFD simulations, and an angular velocity of tip speed ratio of 4 is assumed as the boundary condition. The simulation is then solved, and the resulting output includes stress and displacement values for the rotors.
- The design of a high-quality rotor turbine of approximately 5 kW capacity is achieved by optimizing key aerodynamic parameters.
- A target efficiency of approximately 45% is the target for each two-blade rotor. This target efficiency was chosen based on previous research and industry standards.

2. Literature Review

This section provides an overview of the background of hydropower technology, types of hydrokinetic turbines, the mathematical aspects of power generation, a comparison of the performance of two and three-bladed turbine configurations, design methods, and a review of the key factors that influence the efficiency and effectiveness of these systems. These factors include pressure coefficients, which reflect the distribution of pressure forces acting on the rotor blades, tip speed ratios, which measure the blade tips' speed in relation to the fluid's flow [16] and the flow behavior on the blade surface, which is the principles of fluid dynamics, specifically Bernoulli's theorem that provides a theoretical framework for understanding the generation of aerodynamic forces on an airfoil. There is an investigation on turbulence models, which account for the complex and dynamic nature of fluid flow, and aerodynamic parameters, which describe the forces on the blades. Lastly, a brief overview of the capacity factor will be provided.

Note, there is no literature of rotor swamping for RHKT to improve capacity factors even though this could lead to a doubling of the capacity factor depending on the river flow velocity variation.

2.1. Background

There has been much interest in alternative energy sources derived from renewable, such as wind, biomass, solar, geothermal, tidal, and river power. Several strategies have been applied to help people obtain affordable electricity[17]. Researchers are exploring technologies for harvesting energy, which includes massive hydroelectric plants[18]. Energy produced by hydropower produces 15 g of carbon dioxide equivalent per kWh, which is 30-60 times less than energy produced by fossil fuels [19]. In the past people

invented certain systems to utilize the energy of moving water streams, such as the waterwheel. In recent years, numerous methods have been developed for capturing the energy of flowing water[20]. RHKT rely on the velocity of water, which is available year-round [21]. Small- scale RHKT are an attractive option since they require low construction costs and do not have dams, therefore they are relatively inexpensive compared to other technologies[22]. In an array of RHKT with a sufficient distance, multiple units can be the most effective in producing energy and supplying it to the grid simultaneously[23].

There is a limited amount of literature available regarding the economic feasibility of RHKT technology[24]. A variety of river turbines have been developed by New Energy Corporation, including 5, 25, 200, and 250 kW in capacity[25]. There are some obstacles associated with RHKT. Depending on the type of turbine a minimum flow speed of 2 to 3 m/s is typically required, operate in winter, and the river be free of debris. Due to these problems, adaptability of these technologies is difficult [26]. Currently, RHKT technology development is in the pre-commercial phase. It is true that wind turbines have undergone significant development over the last 50 years, but RHKT needs to be improved for commercialization. Figure 4 shows the commercialized RHKT by various companies[27] showing RHKT with various efficiency and capacity factors.

RHKT has received limited research and development attention other that for rural electrification[28]. As shown in Table 1, Pankaj Kumar Yadav has prepared a list of hydrokinetic turbines that are currently being developed for low-speed applications. The illustration shows a variety of RHKT. Currently, there are only a few horizontal-axis turbine projects in progress, and there are no projects that utilize very low flow rates with

both high-capacity factors and high output powers.

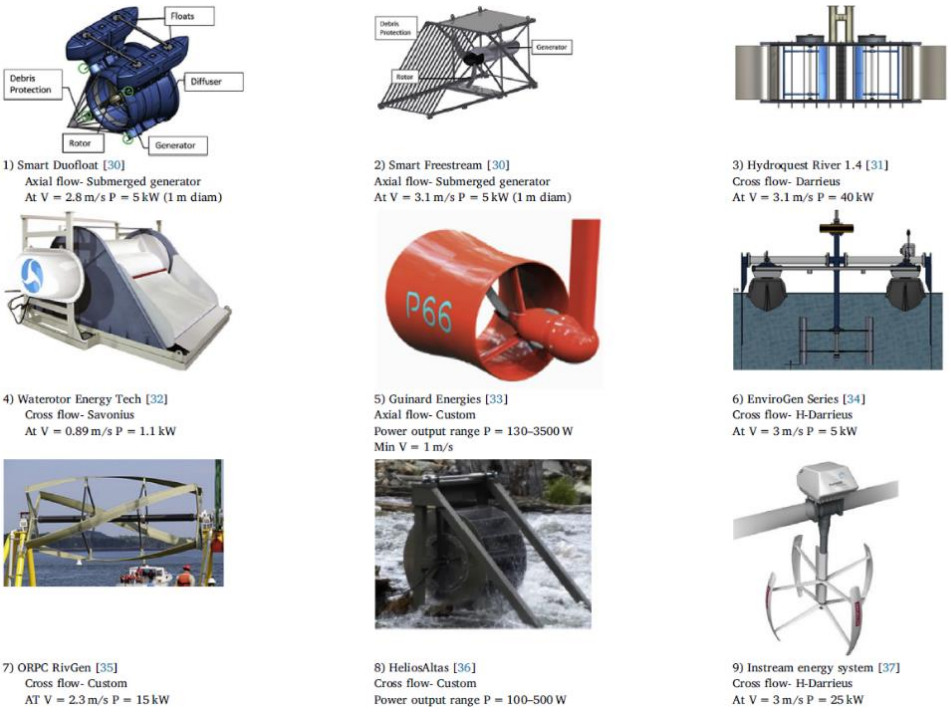

Figure 4: Various commercialized RHKT

Table 1: Various current hydrokinetic project [28]

S.N.	Manufacturer	Device name	Type of turbine	Min/max speed	Output power	Diameter (m)	Height (m)
1	Alternate Hydro solution Ltd. Canada	Free stream Darrieus Water Turbine	Cross axis	(0.8 m/s)/it depends on the diameter	1 to 3 kW	2.5	2.5
2	Seabell int. co. ltd (japan)	Stream	Dual cross axis	(0.6 m/s)/no limit	0.5 to 10 kW	Data not available	Data not available
3	Lucid Energy (USA)	Gorlov helical turbine	Helical Darrieus turbine	(0.6 m/s)/no limit	Up to 50 kW depending on the size	1	1
4	Thropton energy service (UK)	Water current turbine	Axial flow propeller	(0.5 m/s)/it depends on the diameter	2 kW	1.8	-
5	Electric Energy Ltd. (UK)	DuoGen	Axial flow propeller	(0.9 m/s)/(4.6 m/s)	100 W	0.31	Data not available
6	Electric Energy Ltd. (UK)	SailGen	Axial/Horizontal	3–4.1 m/s	125–280 W	Data not available	Data not available
7	Tidal Energy Pty. Ltd. (Australia)	Davidson Hill Venturi (DHV) Turbine	Cross Flow Turbine	1–2 m/s	0.77–6.16 kW	1.5	Data not available
8	New Energy Corporation	Current 025 Series	Cross axis	2.4–3.0 m/s	25 kW	4.8	2.4
9	New Energy Corporation	EnviroGen 005 Series	Cross axis	3 m/s	5 kW	1.5	0.75

2.2. Hydrokinetic turbines

RHKT are categorized as horizontal and vertical-axis turbines[29]. In comparison with vertical axis turbines, horizontal axis turbines have some advantages. These include a lower cut-in wind speed, higher efficiency, more excellent speed range, faster self-starting, and less torque variation[30]. A comparison of characteristics of two common current energy conversion systems can be found in Table 2[27].

Table 2: Comparison of general characteristics of RHKT for horizontal and vertical axis

General characteristics	Horizontal axis turbine	Vertical axis turbine
Minimum operating current velocity	0.5 m/s	1 m/s - need higher velocity to self-start
Operating tip speed ratio (TSR)	Faster (TSR up to 4.5)	Slower (TSR below 3)
Coefficient of power C_p	46%	35%
Water to wire efficiency	25% (calculated) due to less efficient transmission and generator	26% (claimed) due to efficient transmission and generator
Debris resistant	Poor	Good
Torque ripple	Smoother	Pulsating
Rotor simplicity	Fairly complex	Simple
Material quantity and cost	Less	More
Weight	Less	More
Pontoon	Smaller due compactness	Larger
Mechanical power transmission	Complex	Simple

2.3. Comparison of two blades and three blades turbine rotors

There is a more significant variation in turbulence intensities for two-blade rotors compared to three-blade rotor. Since 2-bladed rotors produce stronger tip vortices, turbulent intensities are higher, particularly at the tip. With higher turbulence levels in the wake, 2-bladed rotors recover wakes more quickly than 3-bladed rotors, especially in the area immediately behind the turbine. As a result of this more rapid wake recovery, it is possible to install turbines closer together which will increase the power density per unit of land. In contrast, the fatigue load could be increased by higher turbulence levels[31]. It is possible for many bladed turbines to overcome torque variations as well as reduce vibration and shaking. However, with an increase in solidity, the tip speed ratio, efficiency, and stalling will decrease. As a result of the trials, the tip speed ratio increases with a

reduction in solidity. Theoretically 2-bladed turbines should have a higher capacity factor which may not translate in the field.

2.4. Horizontal axis river turbines hydrodynamics

The rotor converts kinetic energy into mechanical energy by interacting with the rotor and the water. It is composed of multiple blades attached to a hub, and its design has a crucial role in the turbine's efficiency. To optimize power production, the geometry of the rotor must be carefully considered. Many parameters can affect rotor performance, including tip speed ratio, number of blades, airfoil type, power coefficient, solidity, angle of attack and chord line[32].

The maximum available power of a hydro turbine in water is determined by [33]

$$P = \frac{1}{2}\rho A V^3 \qquad 1$$

To determine the performance of a blade, a variety of techniques can be employed. The aerodynamic load of a turbine can be predicted using mainly two methods. BEMT and CFD. The simulation is generally recommended for detailed design, whereas the BEM is preferred for preliminary design and load estimation[34]. It is common for designers to use BEM during the preliminary design phase and CFD simulation during the detailed design phase. Compared to BEMT, CFD approaches provide more accurate results. Furthermore, a complex turbulence model and many computational grids are required to obtain a reliable result from the computation technique [35]. Conversely, BEMT is a straightforward and effective method for studying rotor aerodynamics[36].

2.4.1 BEM theory

One of the most effective methods to optimize chord and twist distributions is

BEMT[37], [38]. The BEMT has been demonstrated to provide desire accuracy compared to computational costs. The main computational load in most optimization procedures results from the repetitive evaluation of the goal function. As a result, The BEM technique offered accurate prediction near stall zones. This process was both cost-effective and effective in terms of computational resources.

According to Manwell and McGowan, force and torque can be computed using BEM theory. They illustrated that a blade may also be split into X sections, each of which would be independent of the others and define the lift and drag forces[39].

Based on the theory, the turbine is assumed operate as an actuator disc. The actuator disc concept in turbines presents a basic description of the aerodynamic flow. According to this idea, the turbine is an actuator disc, As shown in Figure 5. To explain the idea in terms of momentum theory, some assumptions must be made. For BEM theory to work, the following assumptions must be made:

- The fluid flow should be uniform, incompressible, and homogeneous.
- There are an unlimited number of blades.
- In rotor area, velocity is constant.
- There should be no rotational flow produced by the turbine.

According to Figure 5, the mass of fluid moving through a particular cross section of a stream tube is U_1A_1, where U_1 is the velocity of the fluid equal to free velocity, and A_1 is the stream tube inlet area. The A_d represents the actuator disc area.

$$\rho U_1 A_1 = \rho U_2 A_d = \rho U_4 A_4 \qquad 2$$

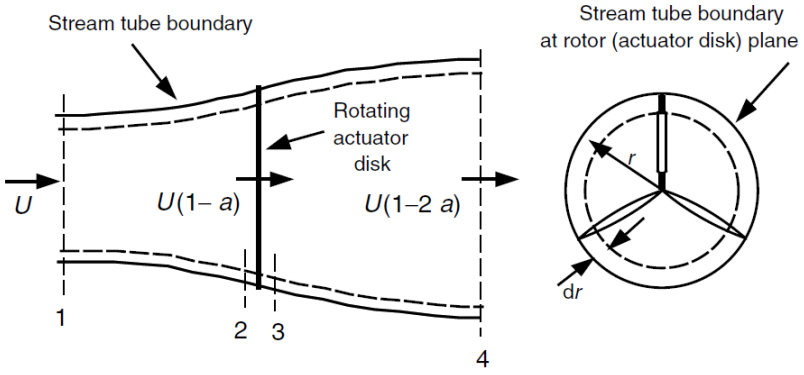

Figure 5: Actuator disc

The axial induced velocity is the difference between U_1 and U_2. This velocity is nondimensional:

$$\frac{U_1-U_2}{U_1} = a \tag{3}$$

The streamwise velocity component U_2 is defined as follows:

$$U_2 = U_1(1-a) \tag{4}$$

Using momentum conservation over the actuator disc describes:

$$(P_2 - P_3)A_d = (U_1 - U_4)\rho A_d U_1(1-a) \tag{5}$$

Bernoulli's equations must be utilized to represent the pressure values:

$$U_4 = U_1(1-2a) \tag{6}$$

The equivalent of this is:

$$U_2 = \frac{U_1+U_4}{2} \tag{7}$$

Power is extracted from the fluid employing Eqn. 5.

$$Power = \mathrm{FU_d} = 2A_d\rho {U_1}^3 a(1-a)^2 \tag{8}$$

$$Power\ Coefficient = \frac{P}{\frac{1}{2}\rho A_d {U_1}^3} = 4a(1-a)^2 \tag{9}$$

The variable of the coefficient of power regarding the induction factor determines

the value of the induction factor that optimizes power:

$$\frac{dC_p}{da} = 4(1-3a)(1-a) = 0 \quad (10)$$

The only physically possible outcome is a = 1/3 because a = 1 leads to $C_P = 0$. Then,

$$C_{P_{max}} = 0.593 \quad (11)$$

In terms of operation, wind turbines and river turbines are similar. Although all kinetic energy can be converted into electricity, Betz's law indicated that 59.3% of that energy can be converted into electricity[13]. Betz Limit refers to this maximum achievable power limit. It is physically impossible for a designer to exceed this limit.

The tip speed ratio is defined by:

$$\lambda = \frac{Velocity\ of\ the\ rotor\ tip}{Water\ flow\ velocity} = \frac{\omega r}{V} \quad (12)$$

As a matter of principle, a tidal turbine's tip speed ratio must be optimized so that as much power as possible can be extracted from it[40]. The power coefficient represents the proportion of the water's potential energy turned into mechanical power. The power coefficient was computed using the fluid's available power in relation to the change in water momentum and the power output[41]. Applying the power coefficient to Equation 1 leads to:

$$P = \frac{\rho}{2} C_P A V^3 \quad (13)$$

Figures 6 and 7 depict the efficiency for the hydrokinetic in numerical and experimental research separately[42].

As a result of the numerical model, TSR 3.48 has a maximum efficiency of 0.42, while TSR 3.77 shows a maximum power coefficient of 43.5% based on experimental results with Stephanie Ordonez Sanchez, as shown in Figures 6 and 7.

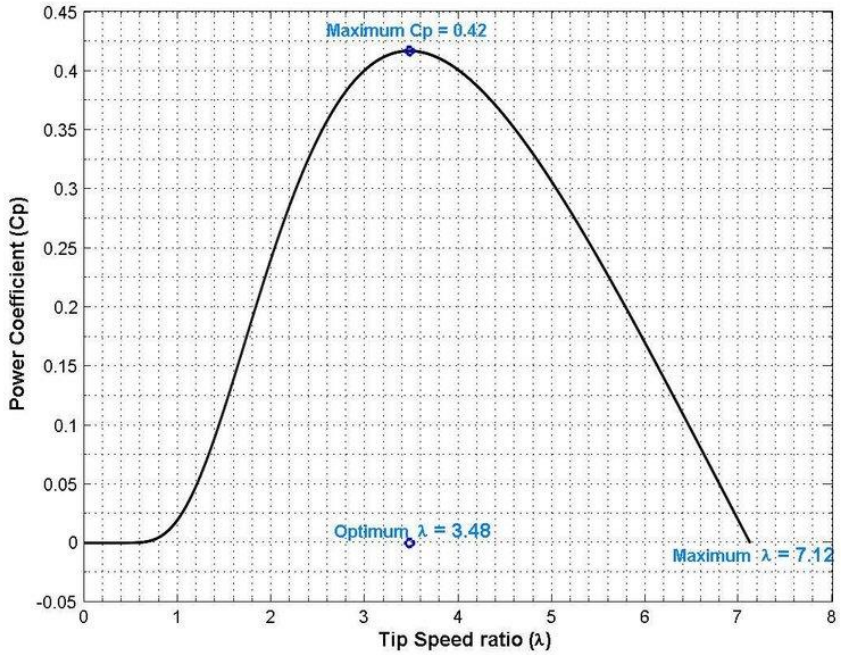

Figure 6: C_p against TSR for river turbine-numerical result

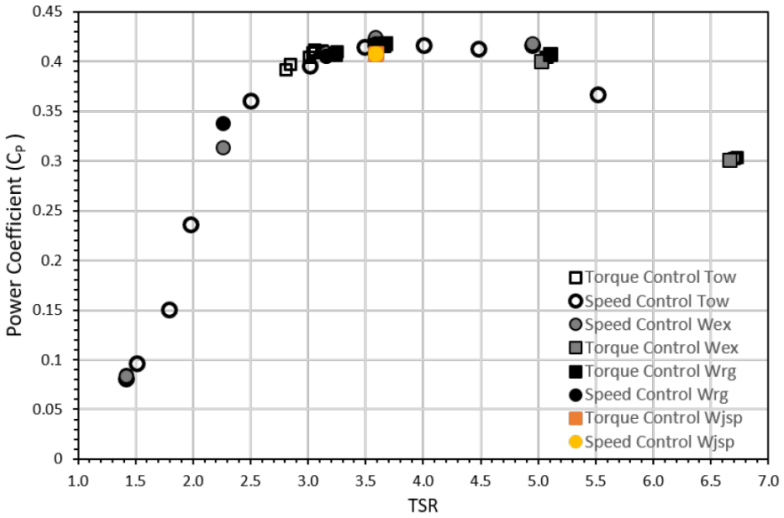

Figure 7: C_p against TSR-experimental result [42]

2.4.2. Airfoils design

In a blade, airfoils are shapes that generate force. There are drag, lift, and torque through the interaction between fluids and blade. Various airfoils topology can be used in the design of turbine blades to generate mechanical power from water. Airfoil function is defined by length and thickness that they are essential for obtaining the mechanical power from the blade. There are various ways to characterize a hydrofoil, as illustrated in Figure 8.

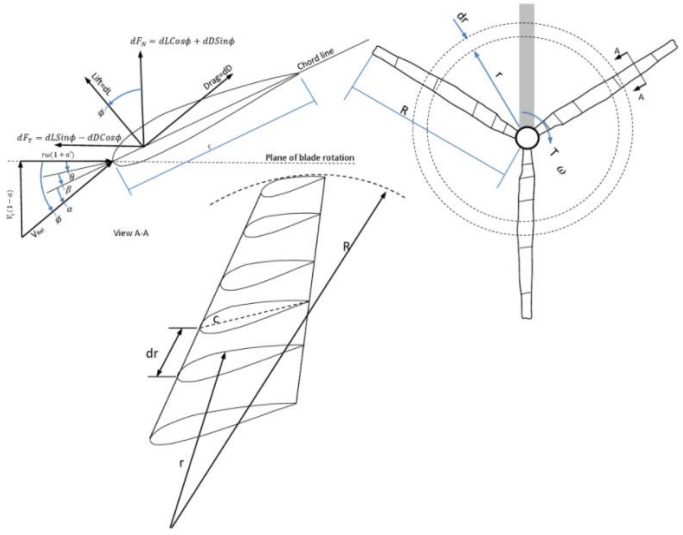

Figure 8: Airfoil characteristics[43]

As seen in the above illustration, the flow velocity on airfoil, chord length, thickness, angle of attack lift and drag force of a hydrofoil are all significant geometric factors that affect the hydrodynamic performance of the hydrofoil.

2.4.3. Turbine blades forces

The hydrofoil's surface is subjected to forces due to the flow of water over its surface. By increasing fluid velocity over the hydrofoils, there is a higher pressure in pressure side compared to suction side. Hydrodynamic forces act on the hydrofoils due to their relative motion in the water. Hydrodynamic forces are generated because of pressure and shear forces. These forces are summarized below:

- Lift force: The lift force is the force perpendicular to the direction of the oncoming flow [44]:

$$L = \frac{1}{2}\rho V^2 A C_L \quad (14)$$

- Drag force: The force parallel to the incoming direction is referred to as drag force. The drag force is caused by uneven pressure distribution on the hydrofoil's top and lower surfaces and by viscous forces acting on the hydrofoil's surface[44].

$$D = \frac{1}{2}\rho V^2 A C_D \quad (15)$$

- Torque force: A pitching moment is the force acting on hydrofoil section that revolves around a perpendicular axis.

The lift coefficient defined as[39]:

$$C_L = \frac{L}{\frac{1}{2}\rho V^2 A} \quad (17)$$

The drag coefficient is defined as[39]:

$$C_D = \frac{D}{\frac{1}{2}\rho V^2 A} \quad (18)$$

and the torque coefficient defined as:

$$C_M = \frac{M}{\frac{1}{2}\rho V^2 CA} \quad (19)$$

A high lift-to-drag coefficient is required to provide a high force for the blade rotation. The drag should be kept as low as possible. The difference in pressure between the two surfaces of the hydrofoil produces a lift force. Overall, a greater attack angle produces a greater pressure difference between the two sides. As a result, it might also result in flow separation on the hydrofoil's suction surface, which would produce drag[45].

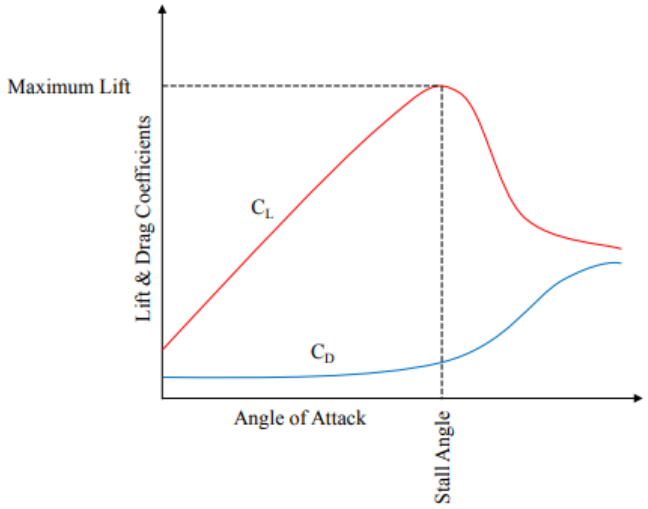

Figure 9: Lift and drag coefficient as a function of angle of attack

A lift-drag coefficient curve is illustrated in Figure 9. As the angle of attack rises, lift force increases linearly until it touches the maximum value. This angle is referred to as the stall angle since it is at this angle that the greatest lift occurs. In contrast, as the angle of attack raises, the drag curve remains relatively flat. When the drag reaches the stall angle, it gradually increases; when it reaches the stall, it suddenly increases.

2.4.4. Flow behavior on the blade surface

The principles of fluid dynamics, specifically Bernoulli's theorem, provide a theoretical framework for understanding the generation of aerodynamic forces on an airfoil. These forces, which include drag, lift, and pitching moments, are produced by the interactions between the fluid and the blade. Specifically, pressure variations on the surface, as well as the resistance or viscosity of the fluid, play a critical role in the generation of these forces. The application of Bernoulli's theorem allows for examining these interactions by analyzing the effect of changes in the velocity of the fluid on the airfoil. Thus, this theorem is an essential tool for comprehending the aerodynamics of airfoils in fluid environments:

$$P + \frac{1}{2}\rho V^2 = constant \quad (20)$$

Bernoulli's theorem states that when the fluid velocity on the leading-edge increases, the pressure decreases, and it leads to negative pressure inclination. Conversely, as the trailing edge, the velocity of the fluid decreases and the pressure, leading to a positive pressure tendency.

An airfoil generates lift force when the fluid pressure is greater on the lower surface than on the upper surface, and the force of gravity is greater than the lift force. Meanwhile, drag force is created by the inequal force on the blade as well as the resistance between the fluid flow and the airfoil[46].

2.5. Turbulence modelling in CFD

Turbulence modeling is a computational approach that allows the calculation of various flow issues using a system of mean flow equations[47]. Hydrokinetic turbine

simulations are conducted using CFD software under turbulent conditions. Different turbulence modelling is frequently used to solve turbulent equations. It should be addressed that these turbulence models must substitute the flow scales instead of necessarily resolving them. The Reynolds-averaged Navier-Stokes models, which time-average the modelled quantities treat variations in a newly introduced quantity known as the Reynolds stresses, are the most widely used turbulence models in engineering[48].

2.5.1 Turbulence models

2.5.1.1 k- ε model

The commen model in CFD for analysing and modelling turbulent flow is the k-epsilon model. The conservation equations are described by two equations in the turbulence model, k and epsilon. This model provides a higher level of robustness for high Reynolds flow than the mixing length model[49].

2.5.1.2 Wilcox's k- ω model

There has been a significant development in two-equation turbulence models. One of the earliest models that incorporate turbulent kinetic energy as one of the transport variables is Wilcox's. The second transport variable, often known as the frequency of the turbulence, is the remarkable dissipation per unit of kinetic energy[47]. In addition to its ability to be integrated across walls, this model does not require a wall-damping function. The origin of this model go back to the work of the scientist Andrey Kolmogorov who first proposed the use of the variable omega, defined as a measure of turbulent intensity.

2.5.1.3 Shear stress transport (SST) model

Based on the boundary layer between the eddies and the complete turbulent viscosity, this model is formulated. The reference model provides more accurate result in the far region and has the most reliable k- ε and k- ω effects[50].

2.6. Capacity factor

RHKT face significant challenges in terms of their capacity factor and economic viability. A system's capacity factor is a critical parameter for its economic performance over time. Capacity factor refers to the ratio between average power and rated power (CF)[51] and is highly dependent on river seasonal velocity variations.

3. Methodology

The direct design approach is widely used for designing and analyzing horizontal axis hydrokinetic turbines. It involves the optimization of the turbine design using numerical simulations and optimization. This approach is explained in greater detail in the present study. Additionally, the significance of various blade parameters is highlighted, including total blade height, blade chord line, and twist angle.

To evaluate the performance of the design, CFD simulations were conducted on the turbine's three-dimensional geometry and operating environment. The process of setting up the simulations, including the grid domain characteristics and boundary conditions specification, is described. To ensure the CFD results' validity, mesh sensitivity influence on the analysis’s accuracy was also investigated. This is an essential step in achieving grid independence, which refers to the stability and convergence of the simulation results as the mesh resolution is refined.

An overview of the rotor design, CFD analysis and mechanical analysis process employed in this study is presented in Figure 10.

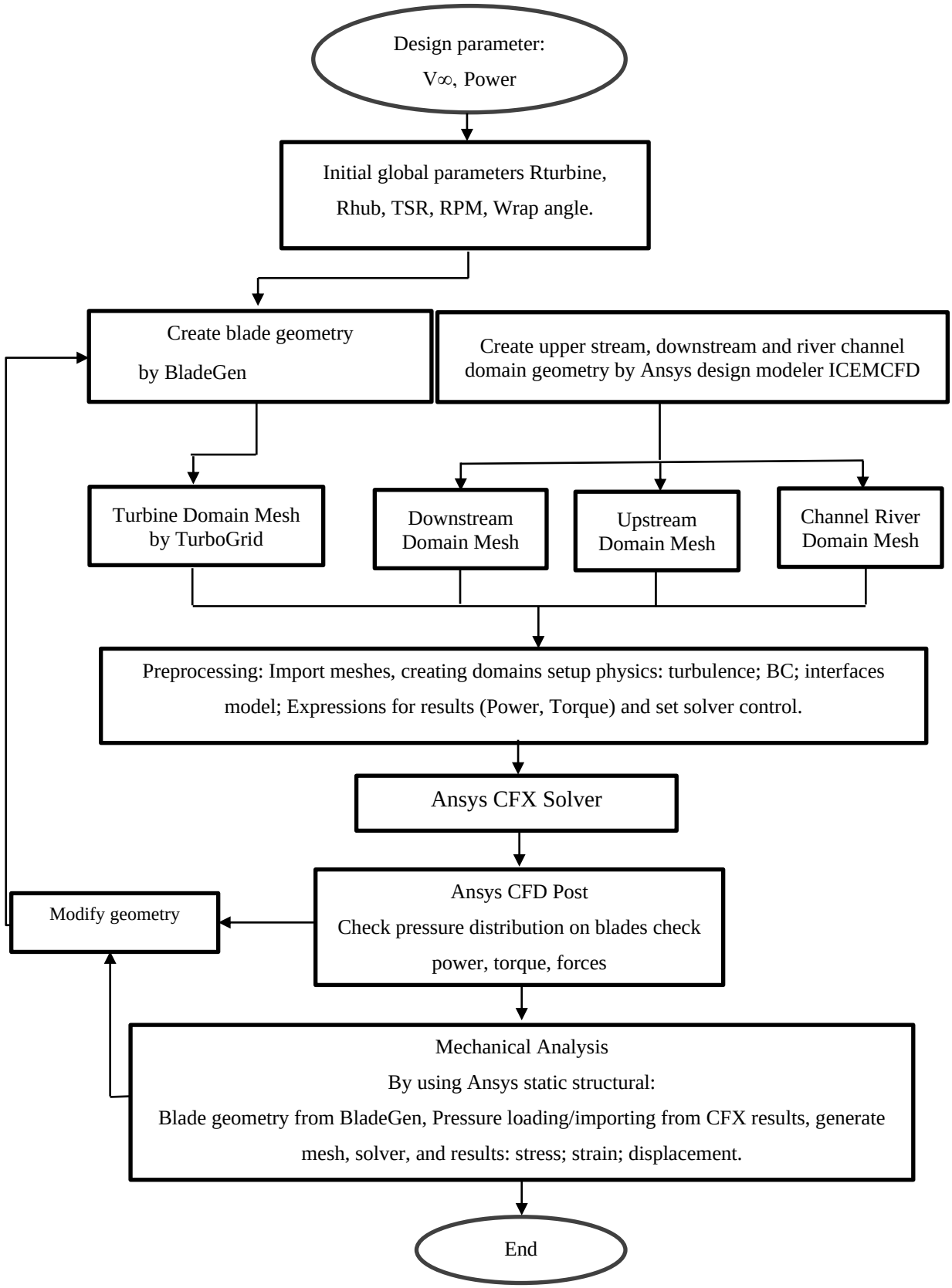

Figure 10: Methodology flowchart to achieve research objectives

3.1 Rotor design

An explanation of the design method used for the 3-D modelling of the rotor is provided. There are several parameters that affect hydrokinetic turbine rotors. These include blade and hub radius (R turbine), total rotor height (Rsh), thickness, and twist angle.

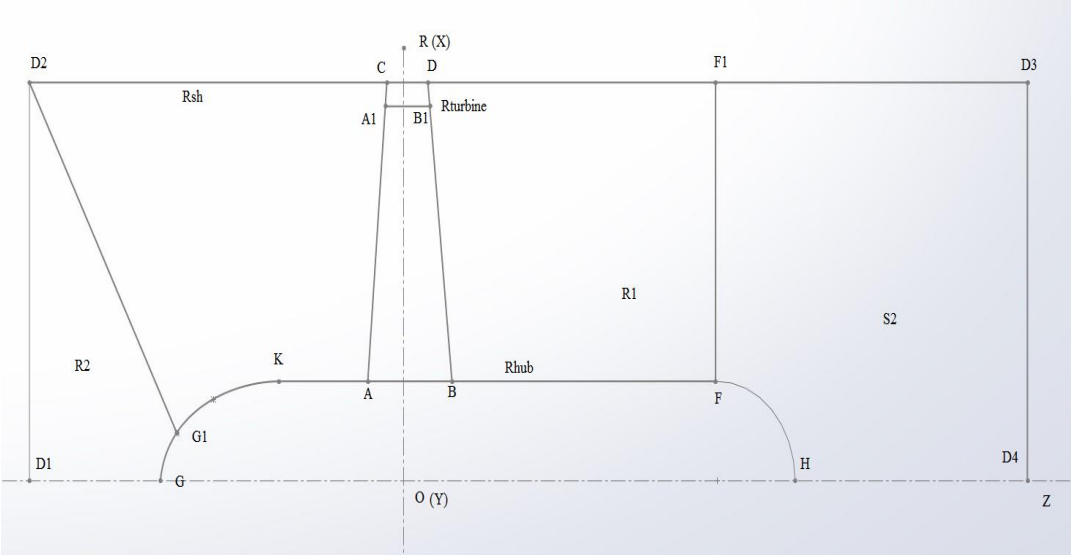

Figure 11: Rotor sketch showing design parameters for the rotor

Defining a blade in three dimensions requires the designer's input. It is essential to consider certain assumptions and requirements during the initial stages of the design process. These inputs are outlined in Table 3. It is planned to achieve an output power of 5 kW, and based on the literature review, the TSR 4 is being considered for the initial design. There are three different velocities for the various seasonal free stream velocities, 1.6, 2.2 and 2.8 m/s, respectively.

Since there are losses in both the generator and turbine, the generator's and turbine's mechanical efficiency must be considered. The generator efficiency is assumed to be 0.96% and the turbine mechanical efficiency is assumed to be 0.97. In addition, a

pressure coefficient of over 40% and below 45% is defined as the design goal.

At the first stage turbine area is calculated to export turbine radius. Therefore, according to the literature review the below equation used to calculate the frontal area of actuator disc for rotors:

$$\frac{P}{\eta_G \eta_M} = \frac{\rho}{2} C_P A V^3$$

The following is the calculation of frontal area of Rotor 1:

$$\frac{5}{0.96 \times 0.97} = \frac{1}{2} 0.4 \times A \times (2.8)^3$$

$$5.37 = \frac{1}{2} 0.4 \times A \times (2.8)^3$$

$$A = 1.223\ m^2$$

According to the calculation, to achieve 5 kW output power after the generator, the hydraulic power is required to be 5.37 kW, considering the loss of power caused by the turbine and generator.

Based on the frontal area a blade radius is calculated:

$$A = \pi r^2$$

$$r = 0.624 \text{ m}$$

As part of the second stage, the following equation is considered for the pressure coefficient (Efficiency):

$$Efficiency = \frac{Turbine\ Power}{Available\ Power}$$

$$Efficiency = \frac{T.\omega}{\rho A V^3}$$

To have the same power available for three rotors, it is essential to increase the frontal area. Table 4 illustrates three different frontal areas for three different velocities.

$$Efficiency = \frac{T.\omega}{13.5}$$

By considering tip speed ratio, angular velocity varies with free stream velocity and turbine radius for three rotors. At TSR 4 the rotational speeds are 43, 94, and 172 rpm for the rotors, respectively. According to the equation, to achieve an initial efficiency of 40%, it is essential to increase the blade torque:

$$0.4 = \frac{T.\omega}{13.5}$$

As torque is directly proportional to the force applied, applying more force will result in greater efficiency. This study aims to increase the force by increasing the optimum blade surface area (not the turbine frontal area) and pressure differences on blade surface by optimizing the aerodynamic parameters.

$$P = \frac{F}{A}$$

$$F = P \cdot A$$

The following figure illustrates the expression used in CFD.

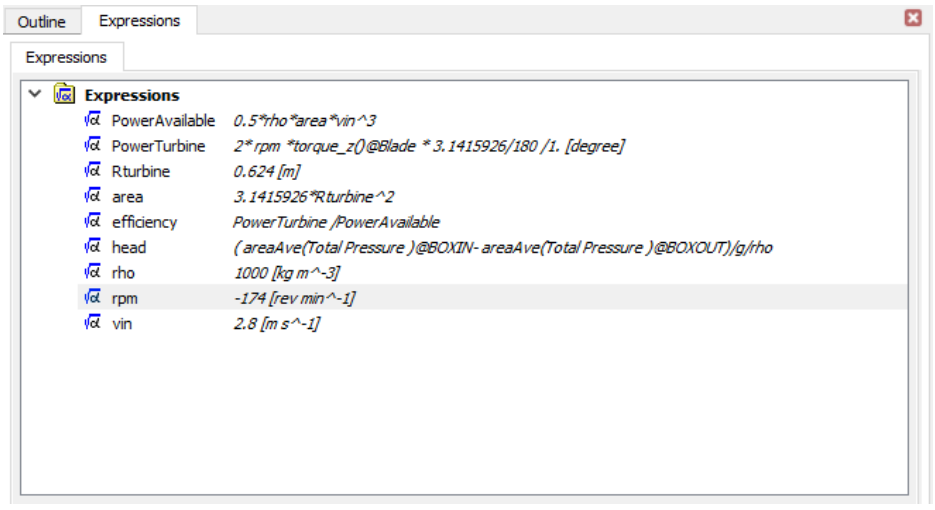

Figure 12: Expression for simulation

Table 3: Design inputs

Rated generator power output [kW]	5	Design goal
Generator efficiency [-]	0.96	Assumption.
Turbine mechanical efficiency [-]	0.97	Assumption.
Turbine hydraulic efficiency [-]	0.40	Design goal
V free stream [m/s]	2.8	Rotor 1
	2.2	Rotor 2
	1.6	Rotor 3
TSR initial [-]	4	Assumption.
Rhub [m]	0.125	Rotor 1
	0.180	Rotor 2
	0.250	Rotor 2

Table 4: Initial design parameters

Power (hydraulic) [kW]	5.37	
Frontal area [m^2]	1.223123178	Rotor 1
	2.521600301	Rotor 2
	6.555175781	Rotor 3
Turbine radius (Rturbine) [m]	0.624	Rotor 1
	0.896	Rotor 2
	1.445	Rotor 3
Shroud Radius (simulation domain) [m]	0.634183673	Rotor 1
	0.910612245	Rotor 2
	1.469387755	Rotor 3

Tables 3 and 4 provide a summary of top-level parameters. An excel spreadsheet is used to calculate absolute velocity, which is defined as the flow velocity relative to the stationary surroundings. Absolute velocity is a measure of the kinetic energy of a fluid. A beta angle is calculated for five blade sections based on the calculated absolute velocity. The following tables present the data for the initial design using the BladGen Ansys module.

Table 5: Blade span airfoil distribution and Beta angle: Rotor 1

Section	r [m]	u [m/s]	C_m [m/s]	C_u [m/s]	Beta_LE [Deg]	Beta_TE [Deg]
1	0.125	2.25	2.24	0.87	31.65	45.15
2	0.252	4.54	2.24	0.43	61.43	63.76
3	0.380	6.84	2.24	0.29	71.12	71.86
4	0.507	9.13	2.24	0.21	75.90	76.21
5	0.634	11.42	2.24	0.17	78.74	78.91

Table 6: Blade span airfoil distribution and Beta angle: Rotor 2

Section	r [m]	u [m/s]	C_m [m/s]	C_u [m/s]	Beta_LE [Deg]	Beta_TE [Deg]
1	0.180	1.77	1.76	1.11	20.72	45.19
2	0.363	3.57	1.76	0.55	59.77	63.76
3	0.545	5.37	1.76	0.37	70.62	71.85
4	0.728	7.17	1.76	0.27	75.68	76.20
5	0.911	8.96	1.76	0.22	78.62	78.89

Table 7: Blade span airfoil distribution and Beta angle: Rotor 3

Section	r [m]	u [m/s]	C_m [m/s]	C_u [m/s]	Beta_LE [Deg]	Beta_TE [Deg]
1	0.250	1.13	1.28	1.74	154.32	41.33
2	0.555	2.50	1.28	0.78	53.25	62.87
3	0.860	3.87	1.28	0.51	69.17	71.70
4	1.165	5.24	1.28	0.37	75.27	76.28
5	1.469	6.62	1.28	0.30	78.55	79.05

The airfoils are distributed every 20 percent of the blades, span-wise. It is estimated that approximately 20% of Rsh is the distance between the hub center and the root blade. There is a greater Beta angle at the tips of turbine blades than at their roots, and the root thickness is greater than the tip thickness. As a final step, a hub and blade geometry will be generated using the BladeGen module in Ansys Workbench. Figure 13 depicts rotor geometry.

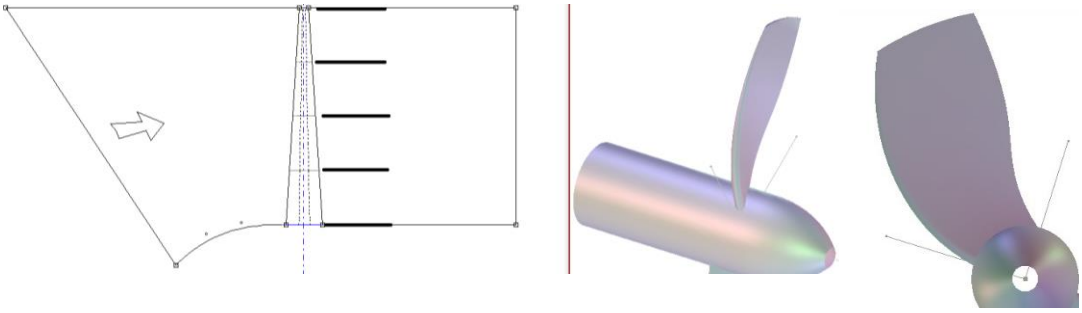

Figure 13: Geometry in BladeGen Ansys Workbench

3.2. Optimization

An optimization method based on genetic algorithms was implemented in the development process of the blade. This method involves using principles of natural selection and genetics to improve a solution iteratively. In this case, the blade was divided into five sections, with each section further divided into ten beta angles for a total of 50 points that needed to be optimized. The optimization process involved incrementally increasing the value of the first point in layer 1, simulating to analyze the results, retaining the optimal point, and then optimizing the second point. This process was repeated until all 50 points were optimized, resulting in an optimum blade. Using a genetic algorithm allowed for a systematic and efficient means of identifying the optimal design parameters for the blade.

3.3. Mesh generation

A cylindrical mesh domain is used to simulate the geometry of turbine blades, considering various critical parameters. The turbine disc, which consists of a circle that lies outside the blades and is designed with high mesh quality to monitor rotational movements accurately, is an integral part of the turbine domain. The turbine domain also includes the entire rotor and is referred to as such to ensure computational accuracy in the simulation process. The

river channel domain surrounds the turbine domain, and upstream and downstream domain meshes are also used in the simulation. The development and implementation of these various domain meshes, including the turbine, river channel, and upper and downstream domains, are described in further detail in the following section. This domain meshes are essential in accurately modelling the flow behavior and function of the blade.

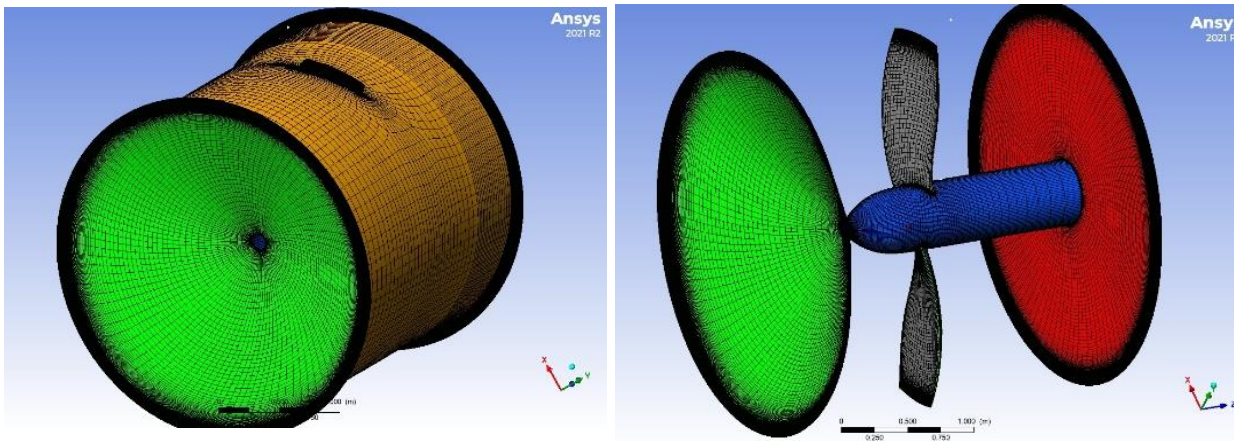

Figure 14: Turbine cylindrical domain mesh

ANSYS Workbench's TurboGrid mesh generator is used to generate a high-quality hexahedral grid on rotors. The quality of the mesh is an important factor in accurately simulating the flow dynamics and performance of the turbine. The mesh sensitivity which will be described in following section is a technique that utilized to minimize memory requirements during the solution process and increase the accuracy of the results. Figure 15 provides an illustration of the mesh quality. To guarantee the validity and dependability of simulation, mesh quality was carefully considered.

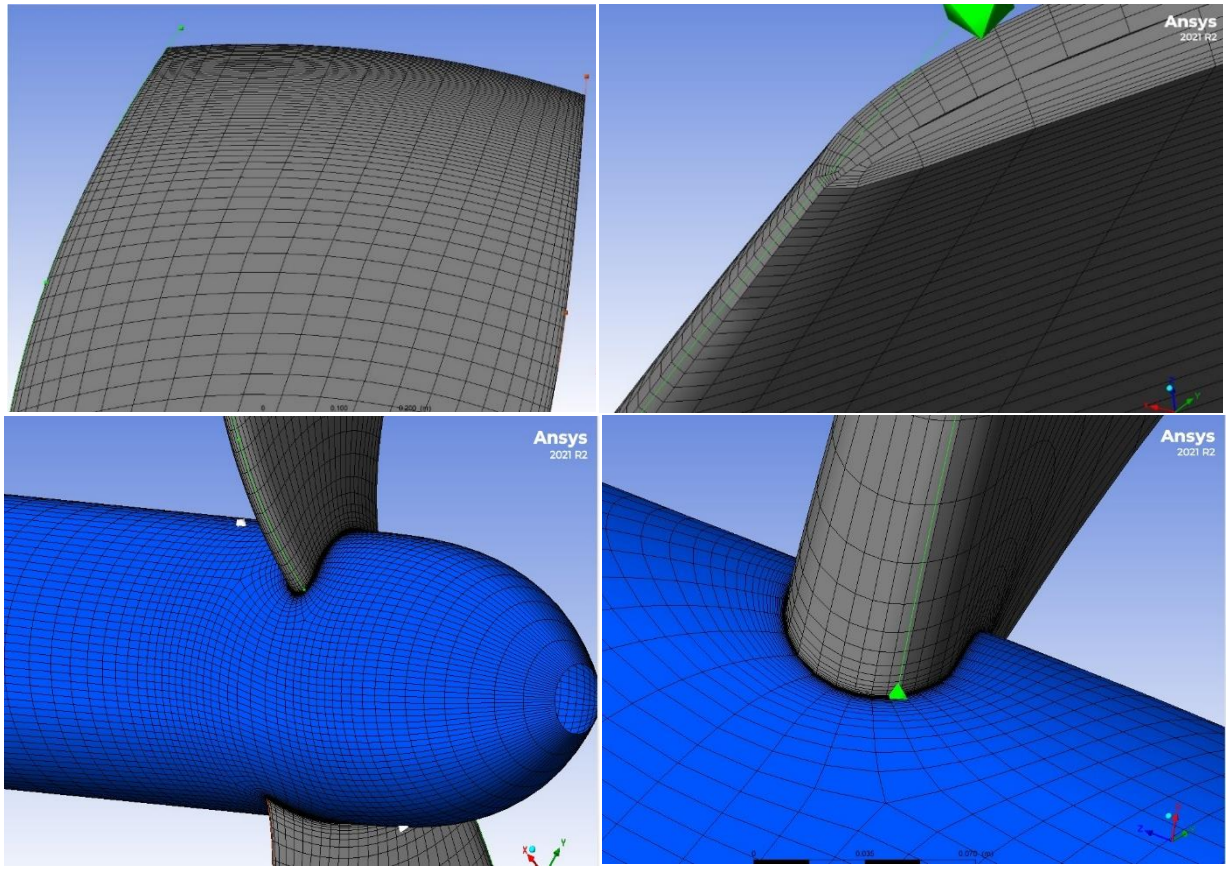

Figure 15: Mesh distribution on blade and hub

A rectangular cube grid is utilized to model the river channel domain, which includes the turbine domain. Three rotors with a blockage ratio of 0.03 are considered in this case. The blockage ratio, which is calculated as the rotor area to channel area ratio, is typically within the range of 0.03 to 0.05. A decrease in the blockage ratio leads to an increase in the volume of water in the model, resulting in more accurate simulation results. The sectional area, width, and depth of the channel for the rotors are calculated using the Table 8, considering the size and configuration of the rotors.

Table 8: River channel domain mesh dimension

Parameters	Rotor 1	Rotor 2	Rotor 3
Blockage ratio [-]	0.03	0.03	0.03
Distance Turbine Tip - Water surface W1-W [m]	1	1	1
Distance Tip to river bottom B1-B [m]	1	1	1
River/channel sectional area [m^2]	40.77	84.05	218.51
Channel Depth C1-C3 [m]	3.2480	3.7920	4.8900
Channel width C1-C2 [m]	12.5526	22.1660	44.6842

The river channel domain depth is determined based on the turbine radius, the distance between the rotor tip and the riverbed and the distance between the turbine tip and the river surface. Thus, the width of the channel can be calculated. A high-quality Hexahedron grid is provided to the ICEM CFD mesh modeler for the creation of the river domain mesh. The turbine domain is in the middle of the box domain as shown in Figure 17. A comparison of the turbine domain to the river domain dimension will assist in determining the appropriate water volume for the modelling to improve the accuracy of the results.

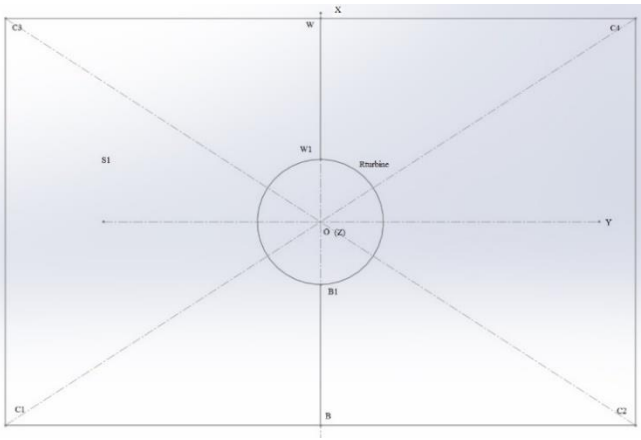

Figure 16: River channel cross sectional area

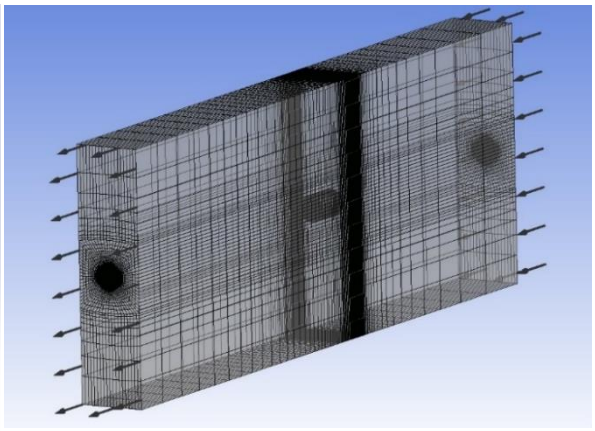

Figure 17: River channel domain mesh

For the CFD analysis described in the methodology flowchart, two more domains mesh are required: an upper stream mesh and a downstream domain mesh. The ICEM CFD Ansys module is used to model a cone for the upstream domain mesh and a cylinder for the downstream domain mesh. Based on the simulation, the upstream domain is rotational, while the downstream domain is stationary.

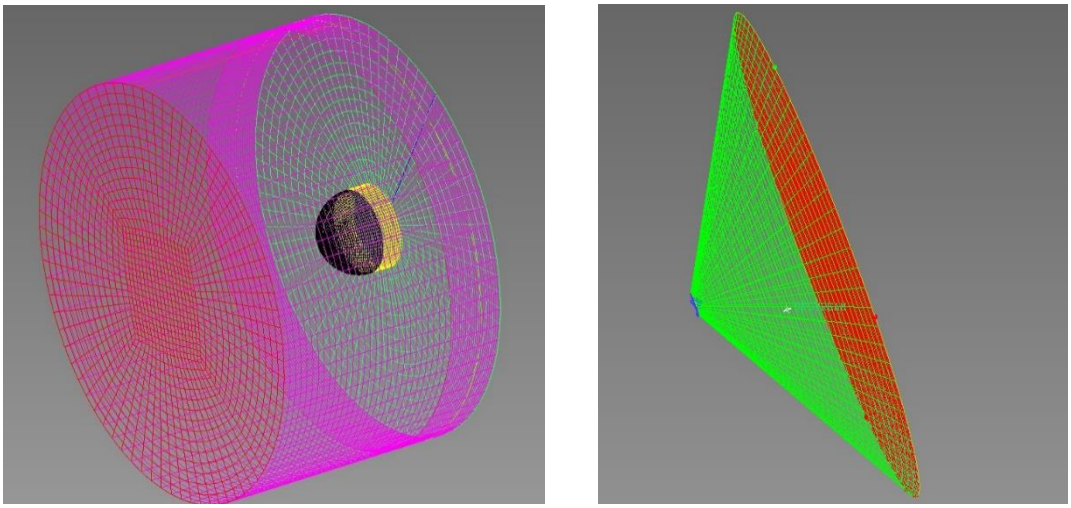

Figure 18: Domain mesh: (a) downstream, and (b) upstream

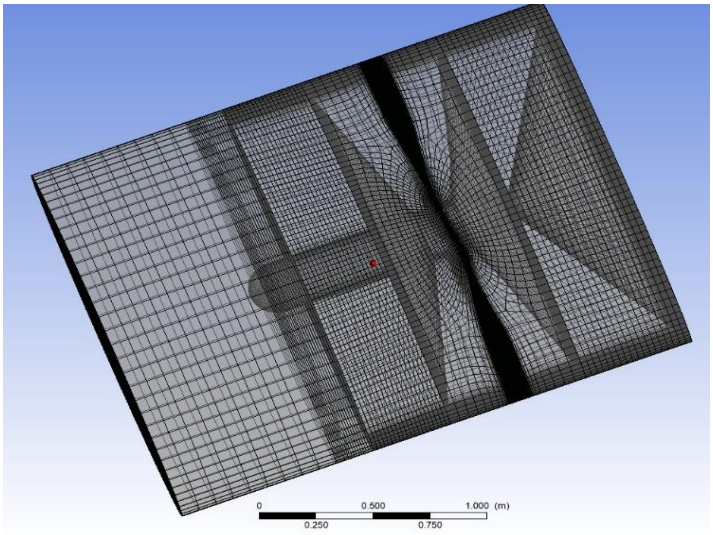

Figure 19: Upstream, downstream and turbine domain mesh

3.3.1 Mesh sensitivity

Mesh resolution significantly impacted CFD results in this study. As a result of the grid convergence investigation, the most appropriate mesh was selected for the subsequent numerical analysis regarding computation performance and results. To conduct the study, SST turbulence models were used to simulate eight different mesh sizes, several elements, and expansion rates. Further, by increasing the expansion rate to two and decreasing the mesh size to the minimum possible size, as well as increasing the number of elements at the tip, the mesh size is reduced to the minimum necessary size. Table 9 shows the mesh settings applied to body surfaces where Mesh 5 was used for the simulation. Compared to other mesh configurations, Mesh 5 had the minor nodes, the highest efficiency, and the most logical iterations. Even though Mesh 7 and Mesh 8 has fewer elements than Mesh 5, there is a residual value exceeding 10^{-4}, which indicates that some nodes were not resolved during the simulation.

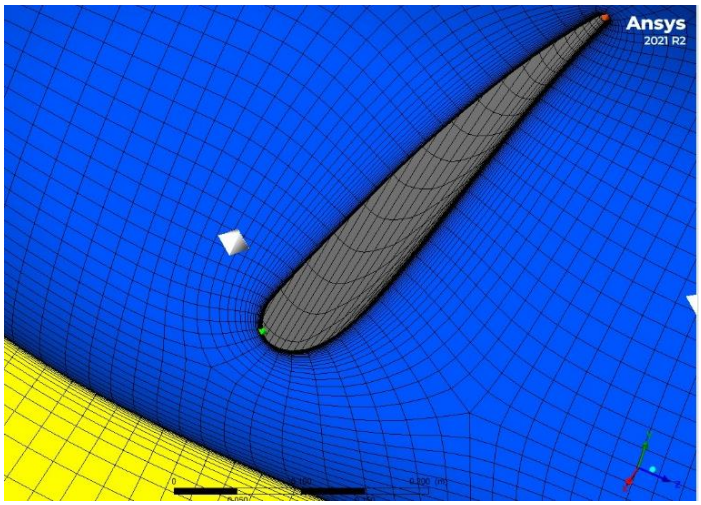

Figure 20: Mesh on hub around blade

Table 9: Mesh sensitivity study

	Number of elements [Root-Between boundary layers-Tip]	Mesh Size [Factor base-Factor ratio]	Expansion Rate	Number of Iterations	Number of nodes for each blade	Efficiency%
Mesh 1	30-70-80	4.05-1.54	1.579	441	1,579,000	42.37
Mesh 2	30-80-90	3.52-1.02	1.5	392	1,500,000	42.57
Mesh 3	30-75-85	3.57-1.09	1.916	528	1,345,000	42.28
Mesh 4	30-80-90	2.5-1.02	1.579	392	1,336,300	42.61
Mesh 5	30-80-90	1.00-1.2	2	401	1,124,000	43.00
Mesh 6	30-80-90	0.8-1.06	2	566	1,086,000	42.44
Mesh 7	20-90-50	1.00-1.2	1.579	Residual value more than 10^{-4}	1,087,000	41.23
Mesh 8	20-98-30	1.00-1.2	1.579	Residual value more than 10^{-4}	1,000,000	40.10

To resolve the viscous sublayer, the inflation mesh is sized so that the non-dimensional first cell height y+ is less than one. A mesh is illustrated in Figure 21 around the blade near the wall.

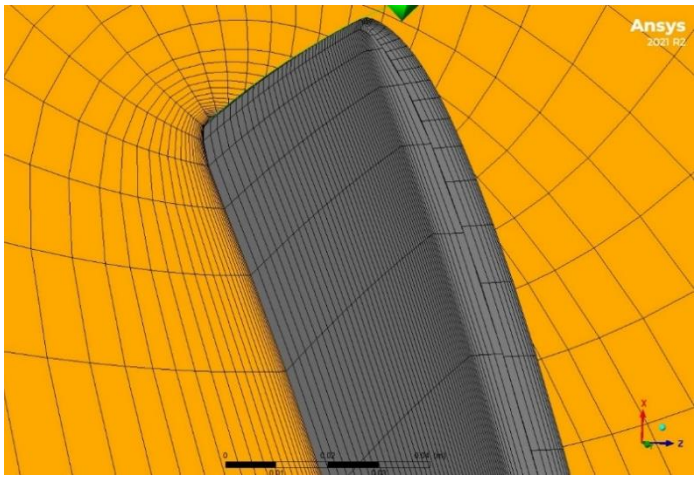

Figure 21: Inflation mesh rate near the wall

3.4 CFD simulations setup

Ansys CFX is used for preprocessing the model. This includes importing meshes, creating domains, and setting up physics such as turbulence models, boundary conditions, interfaces, MFR models, and expressions for the results: power, torque, and efficiency.

The turbine domain mesh, the upper stream domain mesh, the downstream domain mesh, as well as the box or river channel domain mesh are imported into CFX. An example of the upstream, downstream and turbine domain geometry imported into CFX is shown in Figure 22. Various boundary conditions are applied according to the four domains and their defined interfaces.

Upstream and turbine domain motion are rotational, whereas angular velocity is measured in RPM. The SST turbulence model has been developed for these flow domains. In this model, the blade is depicted as a smooth wall with mass and momentum set to no slip. The velocity at a wall is taken to be zero as a non-slip boundary condition, regardless of the roughness of the wall. Although the flow can move along the Slip boundary, the velocity at the boundary cannot be zero. The layer of fluid that sticks to the surface slows the next layer of fluid, slows the next layer, and so on. It is the viscosity between layers of fluid that produces this effect. As a result, no-slip conditions contribute to the development of velocity profiles. The domain motion is defined as stationary for downstream channels and river channels, the remaining two domains.

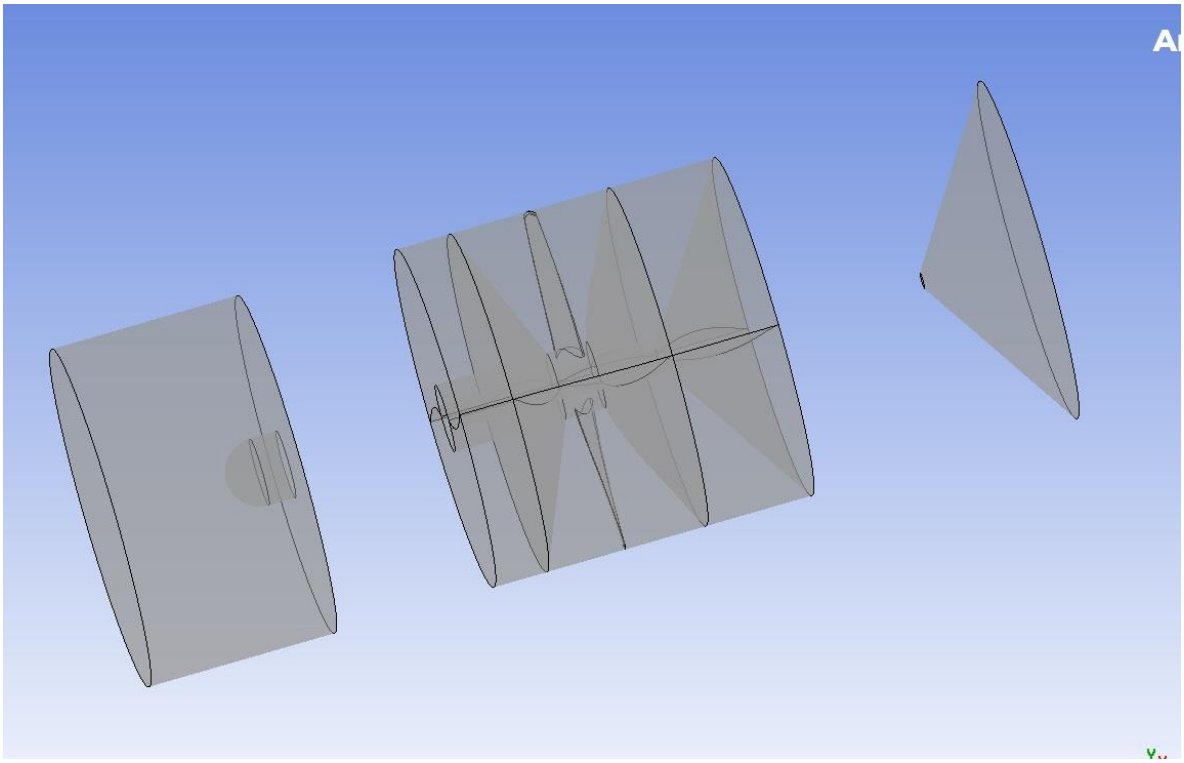

Figure 22: Upstream, downstream, and turbine rotor domain geometry

Mesh connections should be provided for all interfaces between the four domains. Since mesh sizes differ between domains and some domains are rotated, a mesh connection should be set to GGI. Rotating objects, such as turbines, require a generalized grid interface. Figure 23 illustrates that this case consists of two distinct regions, namely two sets of cells. There is a region on side 1 and a region on side 2. As a result of their separation, those two patches could be considered walls. Several issues would arise during the simulation: each zone would be addressed separately without any connection. Once a patch is identified as GGI, the relevant fields are projected from one patch to another.

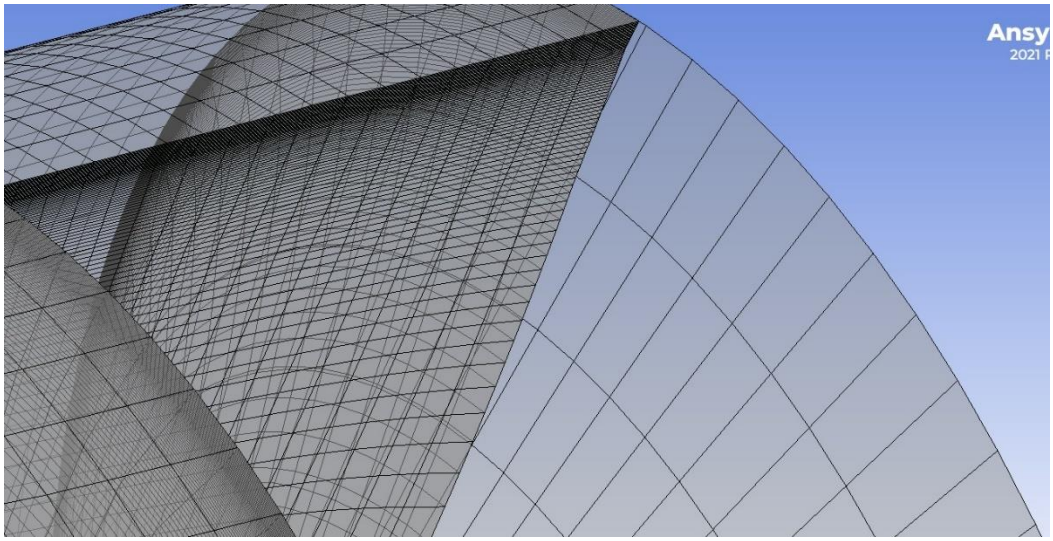

Figure 23: Mesh domains interfaces showing upstream domain and turbine domain

It has been specified that the flow regime at the inlet is subsonic, with an average freestream velocity and a medium turbulence intensity of 5%. Figure 24 shows the inlet and outlet domains. relationship between the fluctuating fluid velocity and the avarage fluid velocity determines the turbulence intensity. It evaluates the intensity of fluctuating fluid velocity. The turbulence intensity at the inlets must be estimated. A few examples of standard methods for estimating the intensity of incoming turbulence are provided below:

High-turbulence case: Inside complicated geometries like rotating gear or high-speed flow (turbines and compressors). The turbulence intensity is 5% to 20%.

Medium-turbulence case: Flow in straightforward equipment such as big pipes, or ventilation flows. Alternatively, in low Reynolds number. There is usually a range of 1% to 5% turbulence intensity.

Low-turbulence case: A low-turbulence case is when a fluid emerges from a fluid, such as air flowing over an automobile, submarine, or aircraft. The turbulence intensity is usually relatively low, typically less than 1%.

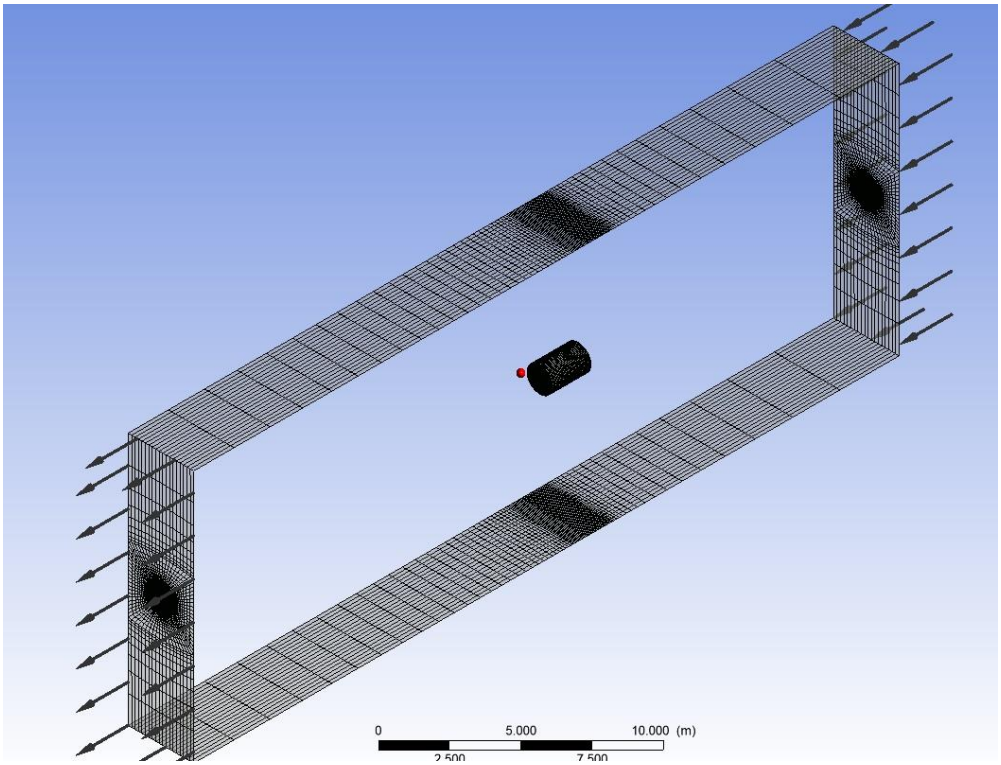

Figure 24: Inlet and outlet in river channel domain

To meet the pressure outlet boundary conditions, static pressure is required at the outlet boundary. Generally, static pressures are used only when the flow is subsonic. It is described that the boxout flow regime is set to subsonic in addition to the average static pressure with a relative pressure of zero Pascal and a pressure profile blend of 0.05. Since the flow is perpendicular and there is no static pressure, only the dynamic pressure is in operation. According to Bernoulli's equation, the flow is either fully developed or the dynamic pressure is constant. The flow at the outlet boundary is uniform.

In contrast, the mean static pressure is more physically accurate since it allows boundary conditions to vary. This typically happens in nozzles (such as diffusers, compressors, turbines, and combustion chambers), where the velocity is greater in the middle and smaller close to the walls. A pressure fluctuation along the boundary is used to represent flow from the inside. In addition, it compels the mass flow to match a typical

value which fluctuates from cell to cell corresponding to the mean static pressure at the entire boundary.

Evaluating the flux quantities at the boundaries of the left and suitable cells is crucial. Because the solution is only known at the average points of each cell which are assumed to be the cell centers, neither conservative variables nor fluxes can be determined at the interface boundaries. As a result of this situation, it is required to develop a method for generating well-posed algebraic equation solutions.

CFD modelling requires the use of equations in the definition of expressions. Several expressions are considered: power available, forces, turbine power, efficiency, area, head, rpm, number of simulations, free stream velocity, and density.

Defining solver control is the next step, which is crucial to ensuring that the results are more accurate. The mathematical technique by which a quantity, such as velocity, is carried through a solution field is called advection. CFX offers three methods of advection. A high resolution, an upwind component, and a specified blend factor. A first-order method called upwind has a lot of numerical diffusions. As a result, the flow is artificially dampened, which causes inaccurate convergence. High-resolution blends to a second-order scheme to preserve boundness when a first-order scheme is impossible. Numerical diffusion is far less prevalent in it. It indicates that the flow is closer to the ideal level of damping since there is less artificial damping. As a result, convergence is slower and less tight because fewer perturbations are present, but accuracy is higher.

The backward implicit Euler's method is a primary numerical method for solving ordinary differential equations. This method is like the standard Euler method but differs in that it is implicit. There is a time-stepping method using a root-finding method to solve the equation: Start with y_0, insert it into Equation 27, and by using root finding, y_1 is

calculated. This process is repeated after obtaining y_1 by using Equation 27 again and finding the root. This is the backward Euler method. This study uses a second-order backward Euler transient scheme as:

$$g(y_{n+1}) = y_{n+1} - hf(t_{n+1}, y_{n+1}) - y_n = 0 \quad (27)$$

There are typically three to five iterations per time step in a transient simulation. These iterations are known as coefficient loops. CFD may require multiple iterations at each time step. This parameter specifies the maximum iterations per each time step. If the convergence requirements are satisfied before this number of iterations, a solution will move on to the following time step. The Navier-Stokes equation's nonlinear component is introduced by updating the linear coefficients since the equations are linearized for each iteration. In the Navier-Stokes equation, the convection term is non-linear because it is multiplied by the velocity gradient. A linear equation solver cannot be used to solve this problem. Linear solvers can solve linear equations by treating the non-linear component as a constant. As a result, the constant is recalculated to model the non-linear component to account for the non-linearity. The coefficient loops are set to 15 iterations per time step.

3.5 Mechanical analysis

Structural analysis of the turbine blades is essential to complete the optimization cycle. The following three causes of damage incidents have been identified: failure of blade material performance, the effects of frequency, and human errors during the installation stage[52]. Due to fluctuating pressure during underwater function, the mechanical forces acting on the blades create cyclic loading.

Optimizing turbine blades typically involves two steps. In the first step, aerodynamically optimal cord line and twist angles are determined along the spanwise direction of blade cross-sections. The second phase involves achieving the ideal mechanical behavior for the correct material blade. A composite material is commonly used in turbines because of its excellent mechanical properties and lightweight[53].

A methodology for analyzing the mechanical behavior of composite materials as blade materials is presented in the following section. There are a variety of conventional materials in use, including metals and composites, while more combinations of composites are currently being investigated. The turbine blades are integral, and researchers recommend using composite materials due to their light weight and stiffness. A polymer composite is selected, and an analysis is performed using a finite element application. As a result, Ansys Static Structural utilizes the finite element analysis method to investigate the characteristics of the turbine blades.

The geometry is exported from the BladeGen Ansys Workbench, and a mechanical analysis was performed. As shown in Figure 25, there is an Ansys Workbench that includes Static Structural and SpaceClaim modeler.

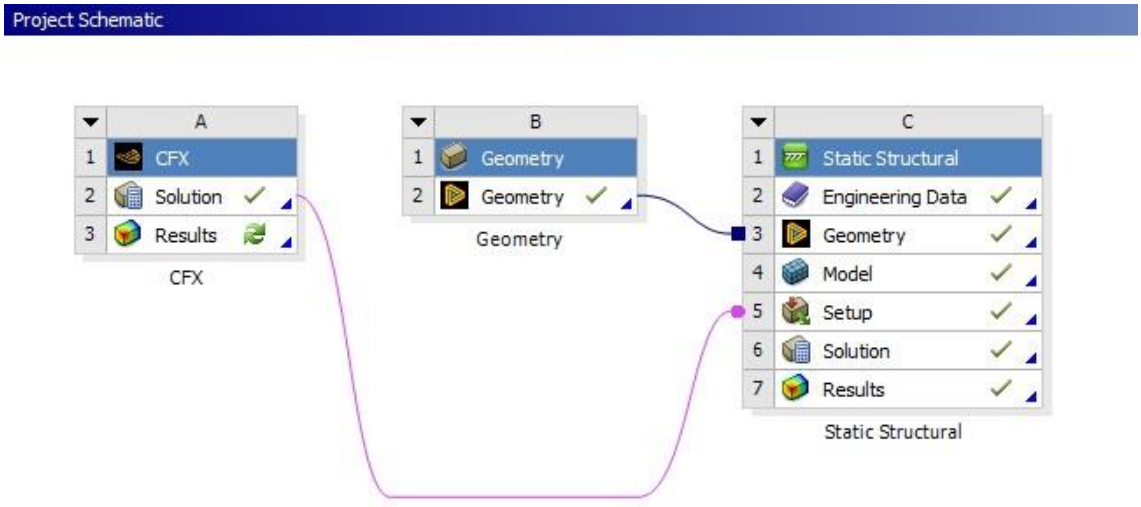

Figure 25: Static structural and SpaceClaim Ansys Workbench modules

Modelling is completed with the boundary condition. The rotational direction is counterclockwise, and the rotational speed of 172 for Rotor 1, 94 for Rotor 2 and 43 for Rotor 3 is defined. Figure 26 illustrates the rotational condition. In addition, Figure 27 indicates that the back hub surface is selected as a fixed surface to fix geometry in the z-direction.

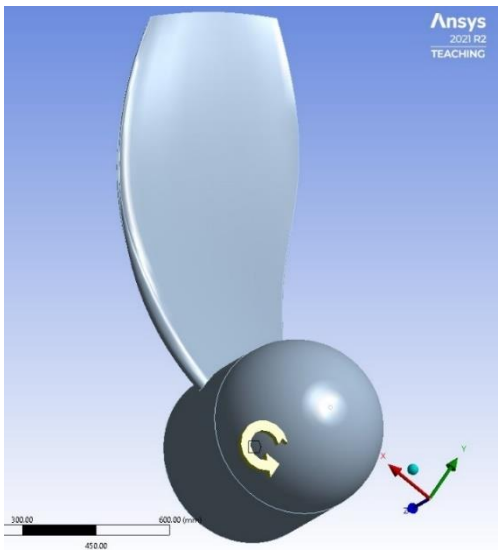

Figure 26: Boundary condition: rotation

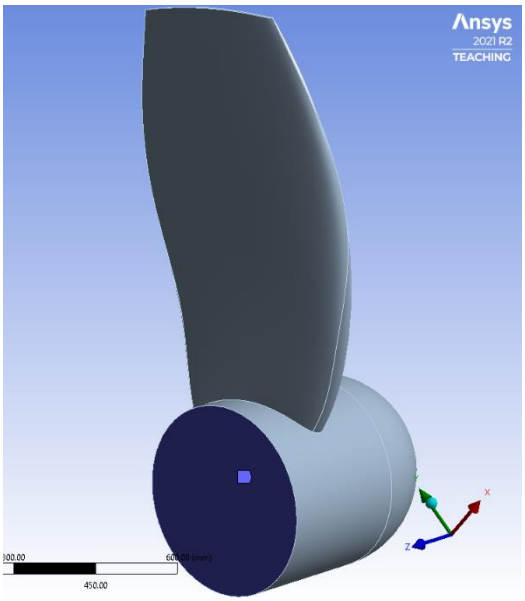

Figure 27: Boundary condition: fixed support

The geometric features were modelled, and the blade was configured with a tetrahedron grid fine mesh. The global mesh density was selected to reduce discretization errors in the failure region.

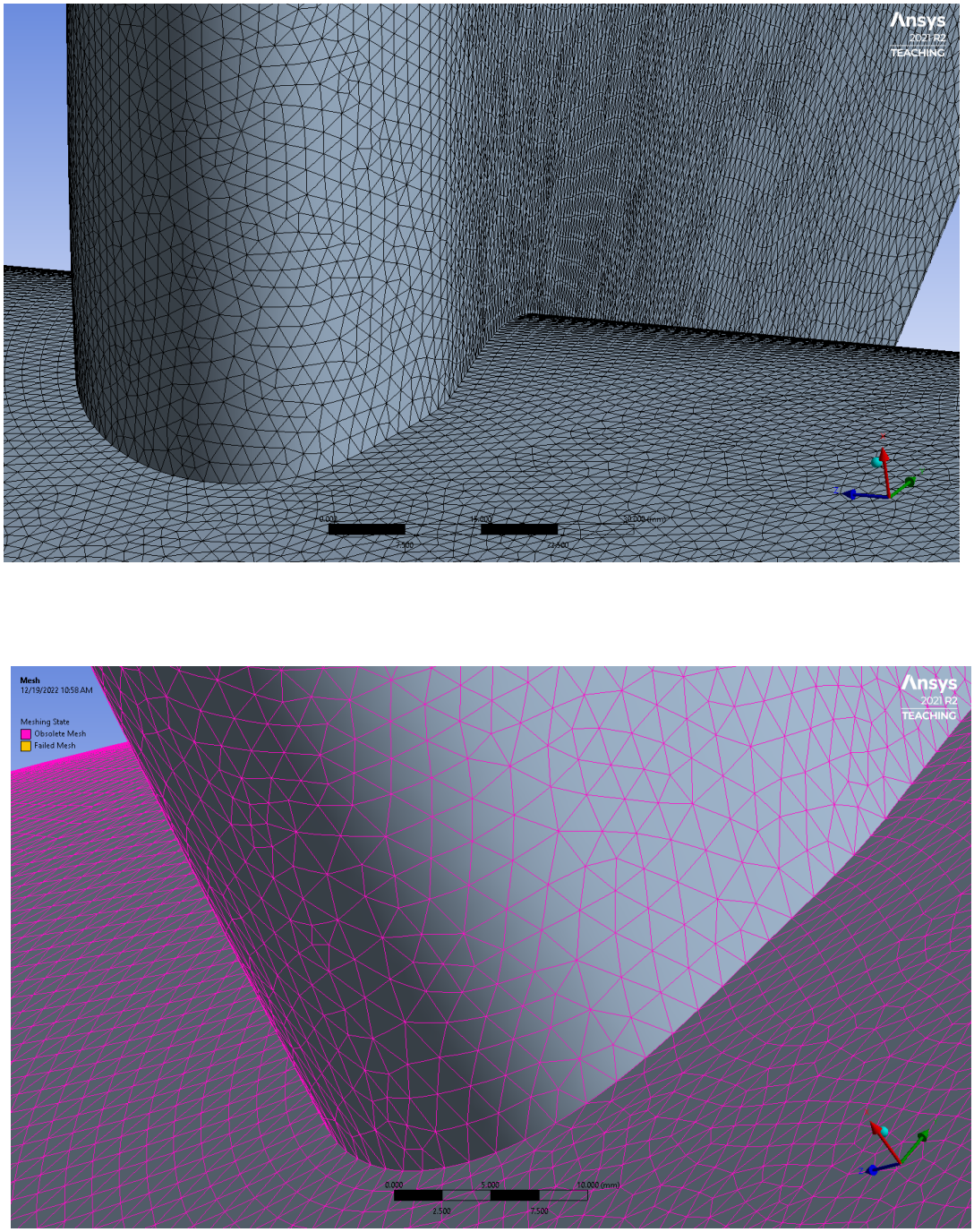

Figure 28: Surface mesh used for rotors

The best option is generally thought to be polymer composites reinforced with long fibres because of their excellent strength, corrosion resistance, and low density. Although carbon fibre and glass fibre are the primary items used for turbine blade strengthening, employing carbon fibre improves performance by minimizing weight and thickness[54].

Study results showed that composites with 30% to 40% fiber loading had higher function. By using nano sized particle fillers, fiber-reinforced polymer composites can potentially have overall performance improved [55]. In Figure 29 the material data is set with material properties such as density, Young's modulus, poison ratios.

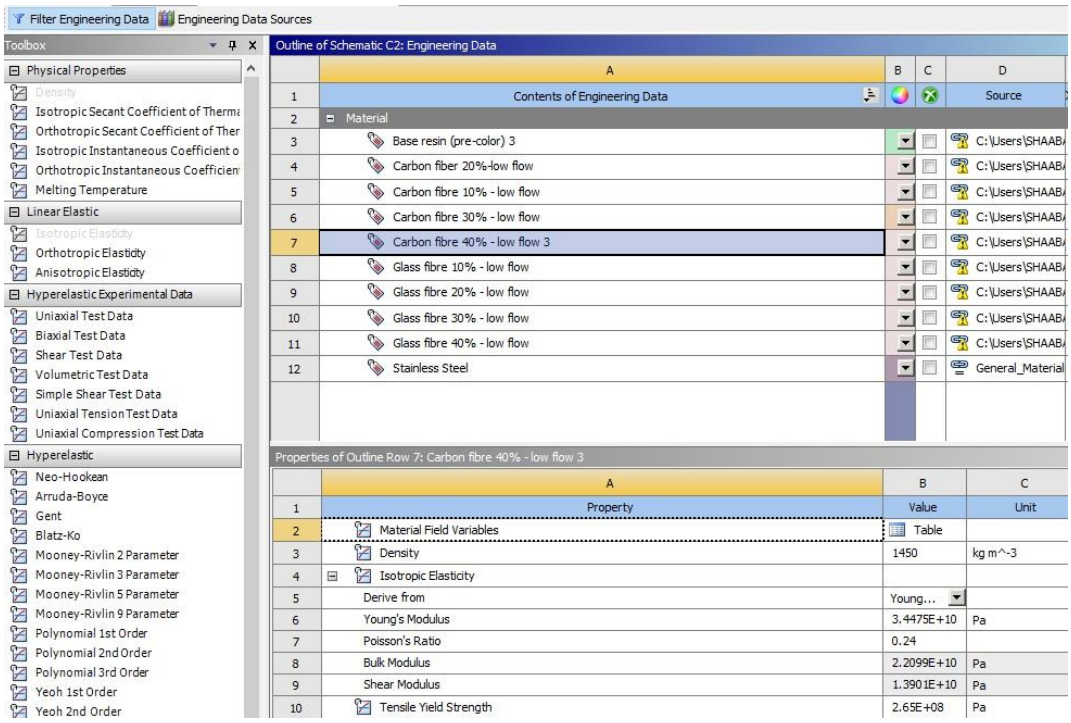

Figure 29: Static structural data sheet: input material properties manually

4. Results and Discussions

This section provides an analysis and interpretation of design and optimization results. Results obtained from numerical simulations of computational fluid dynamics and mechanical analysis are described.

Firstly, the initial design results are investigated to provide insight into the performance of initial topology of blades and assist in any necessary modifications or further optimizations. Secondly, optimum output results were achieved. To determine the rotor, function of pressure, velocity, vorticity, force, torque, and pressure coefficients was examined. Result of the final capacity factor is presented and illustrates how the current study improves the capacity factor. To determine the mechanical behavior of composite materials, mechanical results are presented.

4.1 Initial design results

To design the rotors, an Excel spreadsheet was used to calculate blade radius, absolute velocity, and beta angle (also known as local blade angle). As a result of this angle, local angles of attack are determined. Based on Excel spreadsheet, the calculation data for three different rotors are presented in Tables 10, 11, and 12. During the design process, the rotor radius was divided into five sections, each with an individual beta angle. A first numerical analysis based on an initial beta angle calculated resulted in an efficiency of 11.5%, 13.6%, and 13.3% before optimization.

Table 10: Efficiency before optimization: Rotor 1

	Section	r [m]	Beta_LE [Deg]	Beta_TE [Deg]	Efficiency
Rotor 1	1	0.125	31.65	45.15	11.72%
	2	0.252	61.43	63.76	
	3	0.380	71.12	71.86	
	4	0.507	75.90	76.21	
	5	0.634	78.74	78.91	

Table 11: Efficiency before optimization: Rotor 2

	Section	r [m]	Beta_LE [Deg]	Beta_TE [Deg]	Efficiency
Rotor 2	1	0.180	20.72	45.19	13.63%
	2	0.363	59.77	63.76	
	3	0.545	70.62	71.85	
	4	0.728	75.68	76.20	
	5	0.911	78.62	78.89	

Table 12 :Efficiency before optimization: Rotor 3

	Section	r [m]	Beta_LE [Deg]	Beta_TE [Deg]	Efficiency
Rotor 3	1	0.250	154.32	41.33	13.33%
	2	0.555	53.25	62.87	
	3	0.860	69.17	71.70	
	4	1.165	75.27	76.28	
	5	1.469	78.55	79.05	

In the field of fluid dynamics, momentum analysis is a widely used approach for predicting behavior of fluid flows. The main variables that are typically considered in this analysis are velocity and pressure, as they are integral to the definition of the fluid flow. It is also possible to consider vorticity, which is a measure of the rotational motion of the fluid, as a main variable in momentum analysis.

4.1.1. Pressure distribution

As illustrated in methodology, since force is equal to pressure multiplied by surface area, it is necessary to determine the optimum surface area and pressure distribution to increase the force. There must be sufficient pressure differences on both the suction and pressure sides. As the pressure difference increases, a greater force will be extracted. According to Figure 30, the pressure layers are arranged vertically from the leading edge to the trailing edge. The maximum pressure of +19.36 kPa is located at the leading edge on the pressure side, while the minimum pressure of -32.30 kPa is located at the leading edge on the suction

side. Because -71.73 kPa is located on the blade rather than on the suction surface, it is not considered. The pressure decreases from the leading edge to the trailing edge on the pressure side, increasing from the leading edge to the trailing edge on the suction side. This pressure distribution value results in an efficiency of 40.6%. An increase in the pressure difference is necessary to increase efficiency. A discussion of the role of pressure distribution in increasing force on the blade surface will follow.

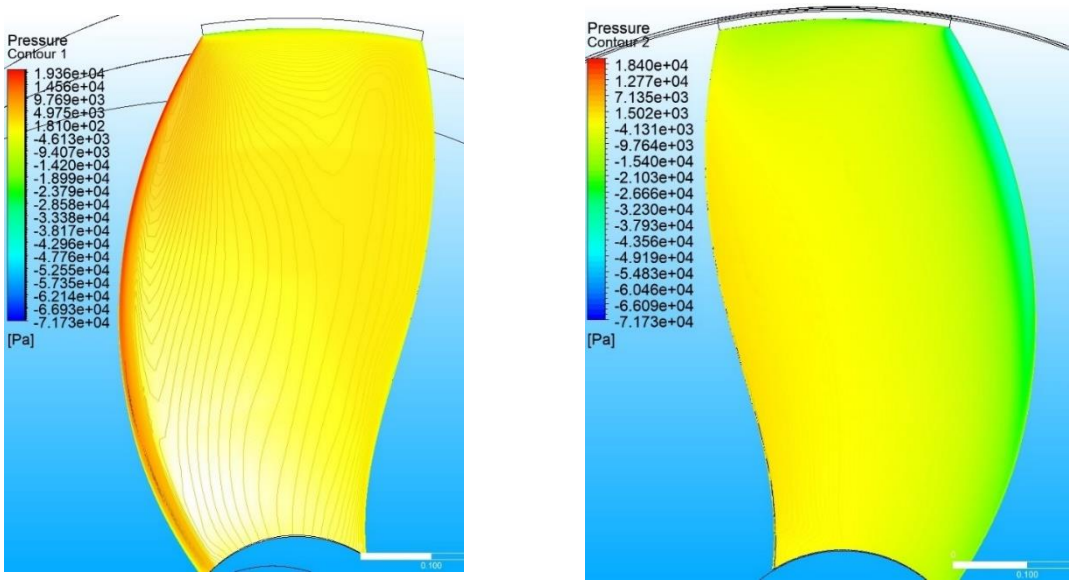

Figure 30: Pressure distribution on pressure and suction side - 40.6% efficiency

4.1.2 Vorticity at tip

The presence of vortices on a blade's surface can significantly impact the pressure distribution. These vortices can produce thin zones of flow reversal and disrupt the steady flow region of separation by causing uneven pressure on the suction surface. These dynamic flow conditions can result in marked pressure fluctuations on the suction blade as the wake passes over it[56]. Evidence of this can be seen in Figure 31, which illustrates the occurrence of pressure fluctuations on the suction side, particularly in regions of higher vorticity. Optimizing the performance of a turbine requires considering the effects of

vortices and pressure fluctuations. As shown in Figure 31, the vorticity is lowest at the middle of the blade on the suction side, and the highest vorticity is at the leading edge near the root of blade.

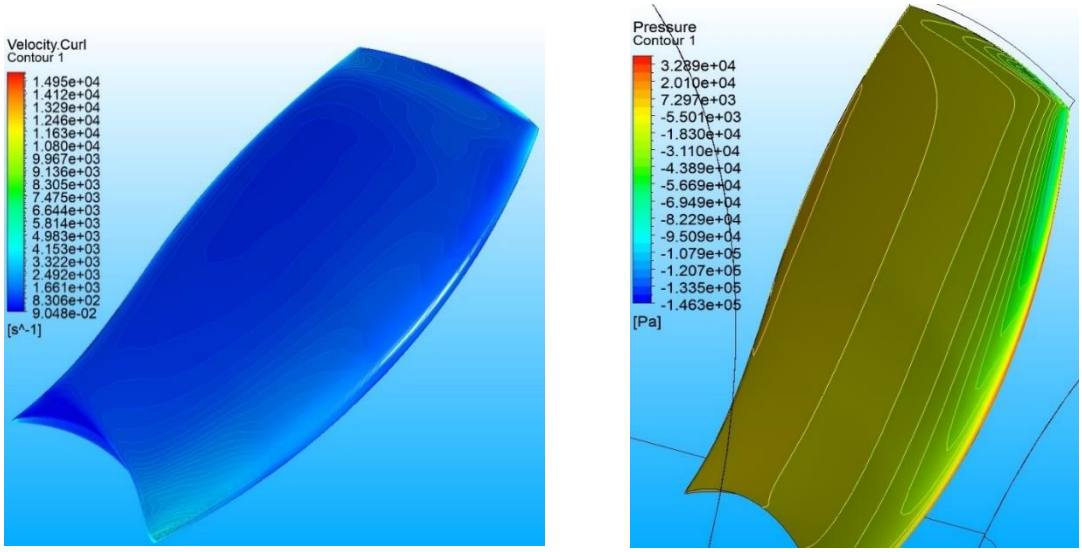

Figure 31: Compare vorticity and pressure distribution on suction side

4.2. Optimization results

The results of rotors' simulations will be presented and analyzed in the following sections. These simulations provide information on the performance of the rotors under different free-stream velocities, and the results can inform any necessary modifications or further optimization efforts. The following data including pressure distribution, velocity, vorticity, forces, torque, power available, turbine power, and efficiency are investigated for rotors.

4.2.1. Rotor 1

Rotor 1 was designed and developed using the Ansys BladeGen and CFX modules to achieve an efficiency over 40% to generate 5 kW of electricity from a 2.8 m/s river water velocity. A pressure contour plot for a free-stream velocity of 2.8 m/s is provided in Figure 32 which illustrates the distribution of pressure on both suction and pressure sides.

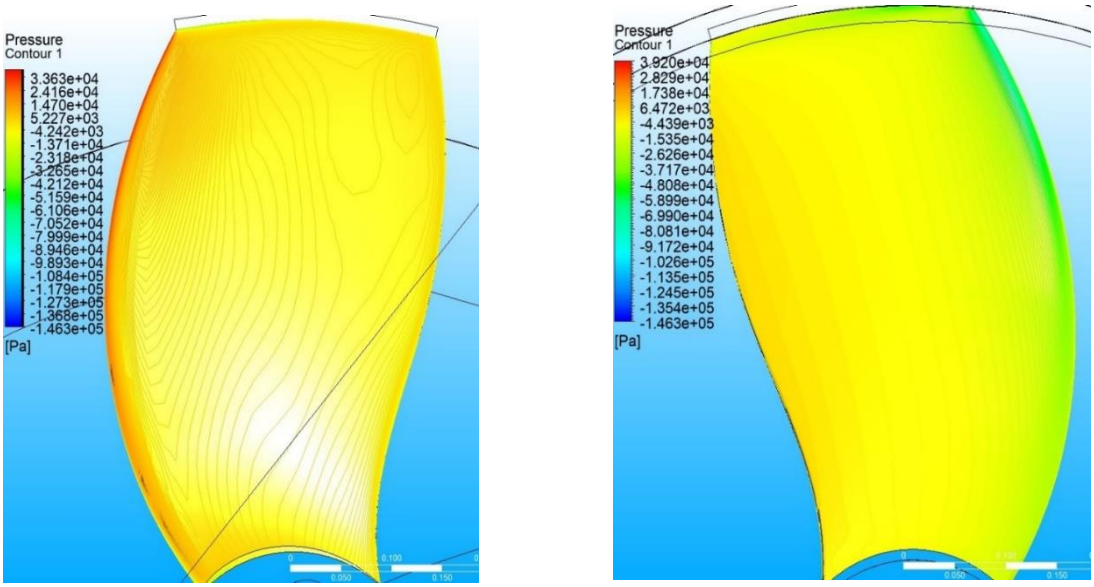

Figure 32: Pressure distribution on surface of Rotor1

As mentioned, the optimization of aerodynamic parameters such as the chord line and Beta angle is crucial for achieving maximum force. Through the optimization process, the maximum pressure distribution on the pressure side leading edge to +33.92 kPa, while the minimum value reached -58.99 kPa. A significant pressure difference is visible on both sides of the blade, extending from the leading edge to the trailing edge. This pressure difference is an essential factor in the overall performance of the turbine.

As a result of these optimization efforts, an efficiency of 45.10% was achieved. Figure 33 illustrates the maximum pressure on the leading edge, while the minimum

pressure is -146.30 kPa on suction side. However, it should be noted that the minimum pressure shown in Figure 34 is not considered in the analysis as it is in a small area near the tip of the blade.

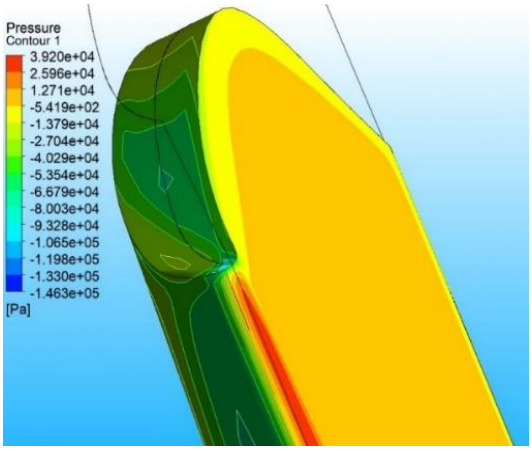

Figure 33: Maximum pressure on leading edge

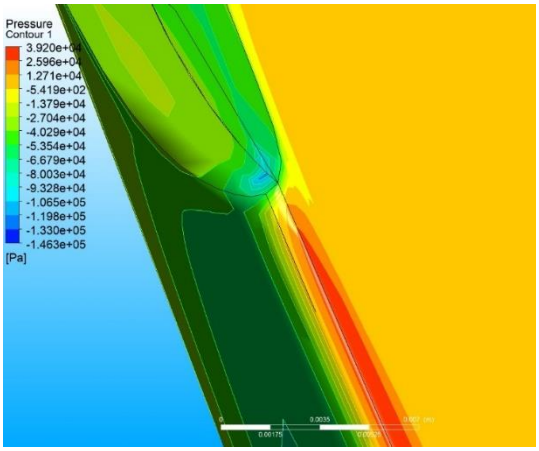

Figure 34: Minimum pressure on top of the tip area

The blades' shape and orientation, the fluid's characteristics, and the operating conditions influence the blade tip's velocity distribution and were considered during the design process. It is crucial to conduct a thorough analysis and understanding of this velocity distribution to optimize the design and operation of the turbine. As illustrated in Figures 35 and 36, observations of the velocity distribution within the turbine domain have revealed a maximum velocity at the blade tip region. This high velocity suggests a pronounced flow of fluid through the blade tip area, which significantly impacts the overall performance of the turbine.

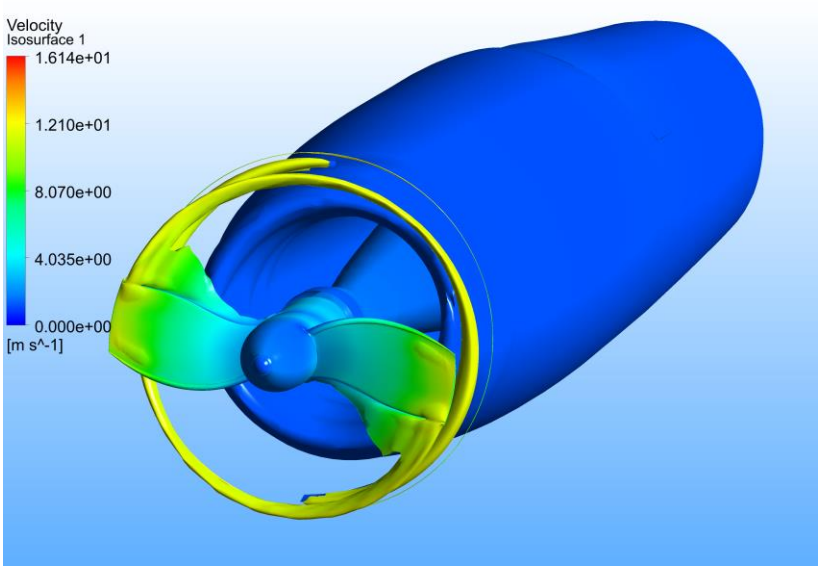

Figure 35: Iso surface velocity contour around the tip area

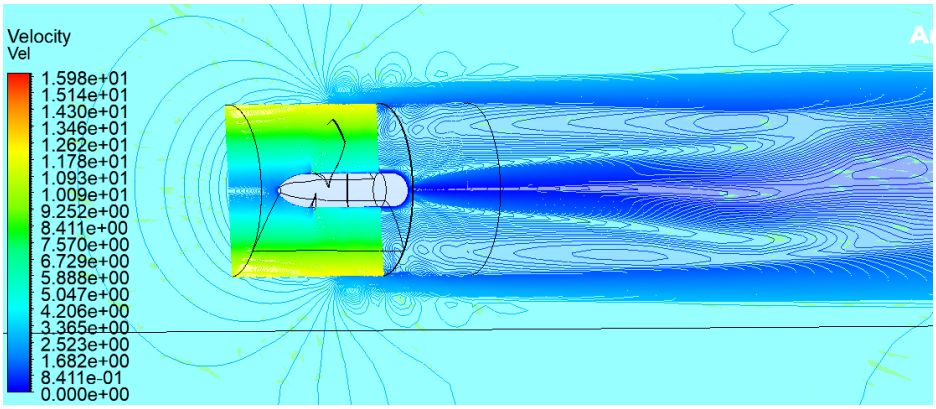

Figure 36: Velocity contour around Rotor 1

Vorticity distribution may have significant implications for the flow dynamics and performance of a rotor and should be considered in the optimization process. Figure 37 illustrates the vorticity on the blade surface of the rotors. Even though Rotor 1 exhibits a small amount of vorticity on its surface, this vorticity has a relatively small impact on the pressure distribution.

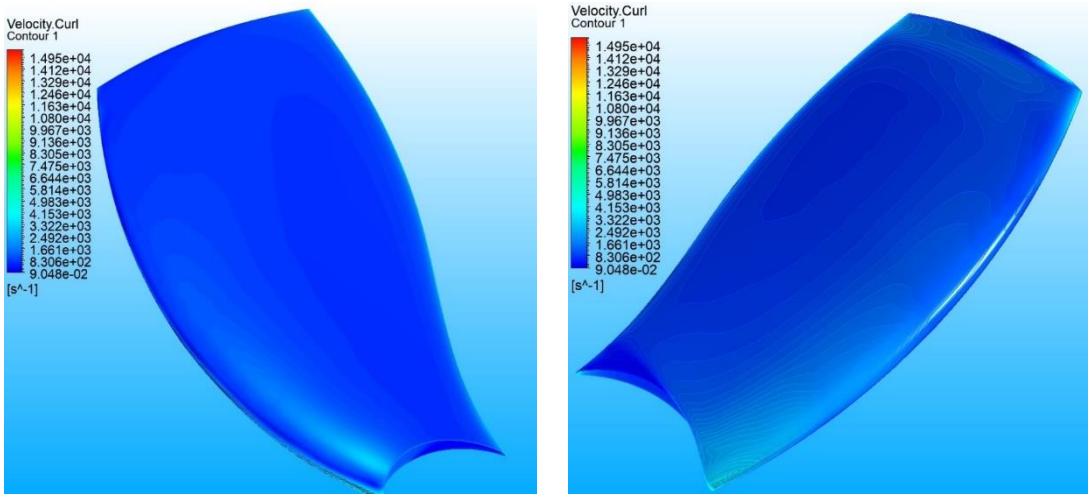

Figure 37: Vorticity on blade 1

Pressure and viscous force are shown in Table 13, as well as pressure and viscous torque. The target output power must be extracted from the blade surface by applying pressure force in the z direction. In this case, z is parallel to the direction of flow. Based on Table 13, a maximum pressure force of 4.29 kN is applied to the blade surface. Viscous forces are negligible in comparison to pressure forces. Consequently, drag forces are close to zero.

Table 13: Pressure and viscous force, pressure, and viscous torque of Rotor 1

Type	X	Y	Z
Pressure Force (N)	0.295	-0.011	4275.20
Viscous Force (N)	0.008	-0.052	10.07
Total Force (N)	0.304	-0.159	4285.30
Pressure Torque (N-m)	0.037	-0.314	-362.85
Viscous Torque (N-m)	-0.003	0.007	26.97
Total Torque (N-m)	0.037	-0.307	-335.88

In accordance with the methodology illustrated in Figure 38, the turbines have a maximum available power of 13.5 kW based on 1.6, 2.2, and 2.8 m/s free stream velocity, water density, and turbine cross-sectional area. Figure 39 illustrates the maximum hydraulic turbine power of 6.0 kW of electricity for Rotor 1. Based on the efficiency of the generator and the mechanical efficiency of the turbine, a rated generator power output of 5.6 kW was determined.

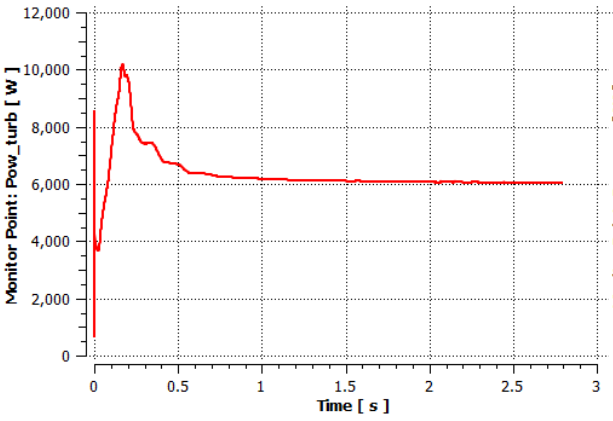

Figure 38: Power turbine of Rotor 1

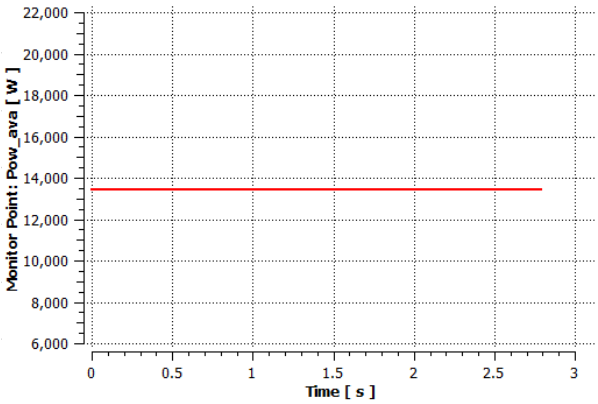

Figure 39: Power available of Rotor1

According to Figure 40, the average efficiency of Rotor 1 is 45.1%, which is calculated by dividing the hydraulic output power by the available power.

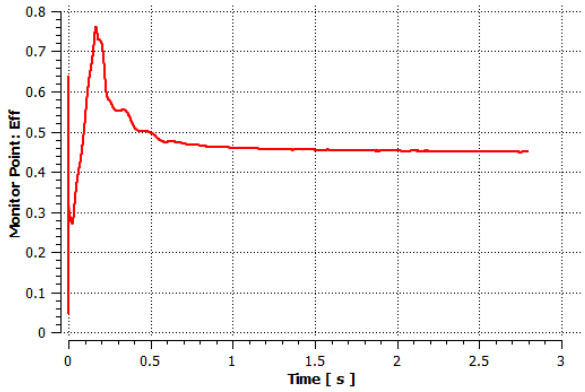

Figure 40: Efficiency of Rotor 1

Following are the optimized beta angles at the leading edge and trailing edges, along with their efficiency values. Presented in the table are values that indicate the optimal beta angles for maximum efficiency.

Table 14: Optimum beta angle of Rotor 1

Section	r [m]	Beta_LE [Deg]	Beta_TE [Deg]	Efficiency
1	0.125	19.53	74.16	45.10%
2	0.252	42.10	80.91	
3	0.380	52.74	83.47	
4	0.507	54.44	85.16	
5	0.634	57.82	88.31	

4.2.2. Rotor 2

The pressure distribution on the blade surfaces of Rotor 2 is depicted in Figure 41. This distribution exhibits a decrease in the maximum pressure on the leading-edge pressure side as one moves toward the trailing edge. Conversely, the minimum pressure on the leading-edge suction side increases towards the trailing edge. These findings highlight the complex nature of the flow dynamics at play and the importance of precise design in maximizing the electricity generation efficiency of Rotor 2.

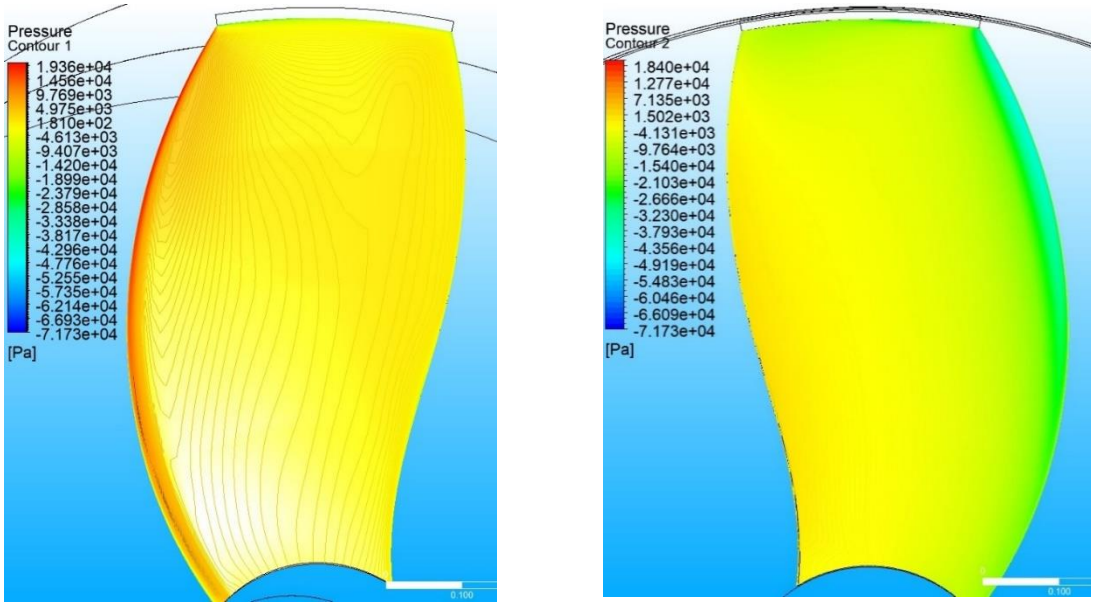

Figure 41: Pressure distribution on surface of Rotor 2

Figure 41 illustrates a pressure contour plot for a free-stream velocity of 2.2 m/s. Based on the optimization process, the maximum pressure distribution on the pressure side leading edge reached +19.36 kPa, while the minimum pressure distribution reached -38.17 kPa. There is a significant difference in pressure on both sides of the blade, extending from the leading edge to the trailing edge. As a result of this pressure difference, the turbine can attain 43.27% efficiency of operation.

The blade tip region of the turbine domain exhibits a pinnacle velocity as shown in Figure 42. A high velocity indicates that fluid is flowing rapidly through the blade tip region, which has a substantial impact on the operation of the turbine.

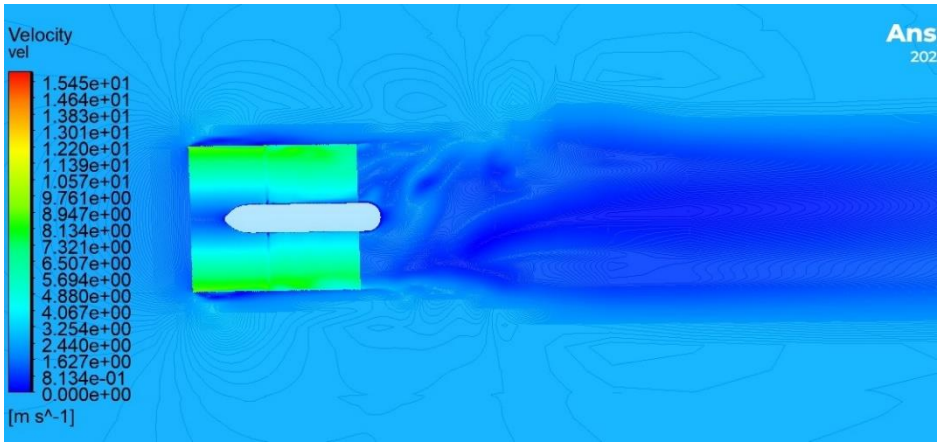

Figure 42: Velocity contour around Rotor 2

Figure 43 provides a visual representation of the vorticity distribution on the blade surface of Rotor 2 following optimization. Despite the presence of minor vortices on the surface of Rotor 1, the surface of Rotor 2 reveals a distribution pattern and peak level like that of Rotor 1. However, it is important to note that the distribution of vorticity on the surface has a limited impact on the flow dynamics and performance of Rotor 2.

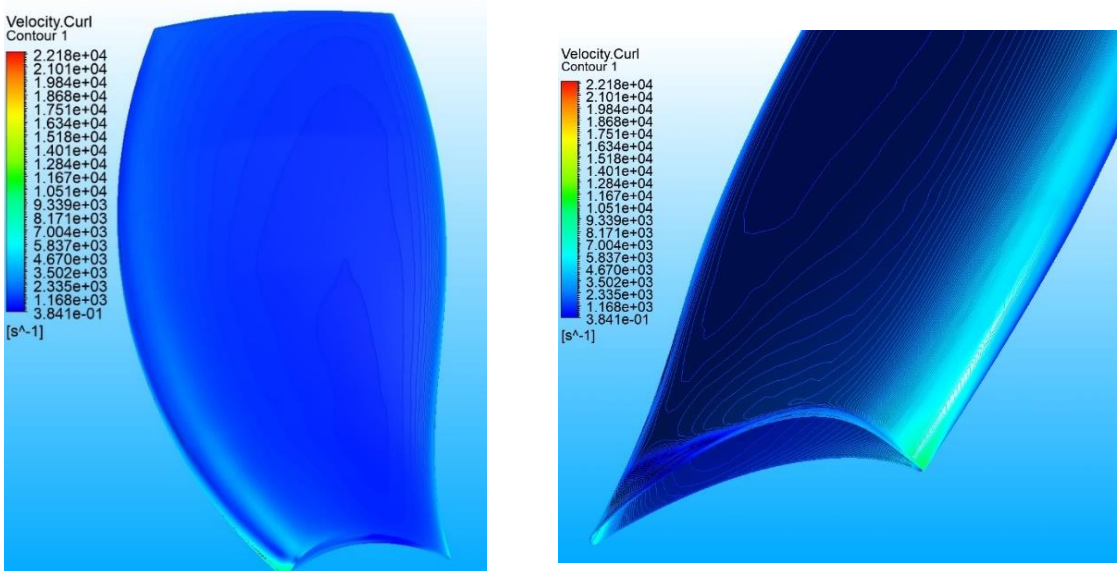

Figure 43: Vorticity on blade 2

In Table 15, pressure, and viscous force, as well as pressure and viscous torque, are presented. To extract the target output power from the blade surface, a pressure force is applied parallel to the flow direction, denoted as the z-direction. According to Table 15, the blade surface is subjected to a maximum force of 5.78 kN. Compared to the pressure forces, the viscous forces are negligible, thus resulting in minimal drag.

Table 15: Pressure and viscous force, pressure, and viscous torque of Rotor 2

Type	X	Y	Z
Pressure Force (N)	-72.235	46.309	5768.60
Viscous Force (N)	-0.356	-0.548	12.08
Total Force (N)	-72.591	45.761	5780.70
Pressure Torque (N-m)	-111.050	148.630	-612.42
Viscous Torque (N-m)	-0.049	0.114	48.12
Total Torque (N-m)	-111.10	148.750	-564.29

Figure 44 illustrates the turbine hydraulic power of 5.8 kW produced by Rotor 2 with the same available power of 13.5 kW. An optimized output of 5.4 kW is obtained with a hydraulic power of 5.8 kW after applying generator and turbine losses.

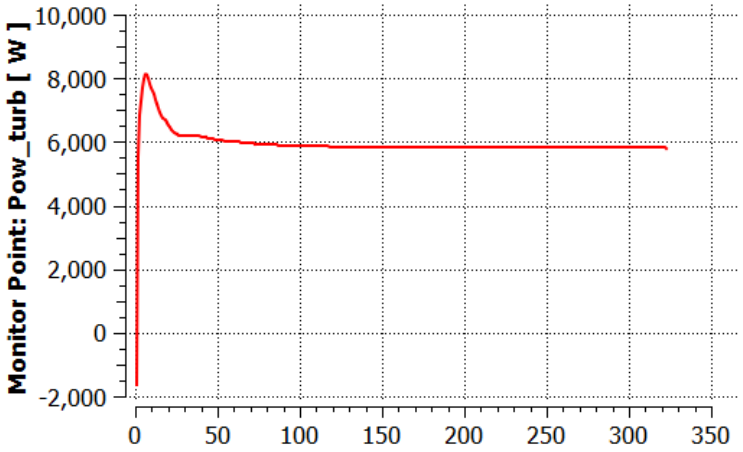

Figure 44: Power turbine of Rotor 2

Figure 45 displays the efficiency of Rotor 2, which is recorded at 43.27%

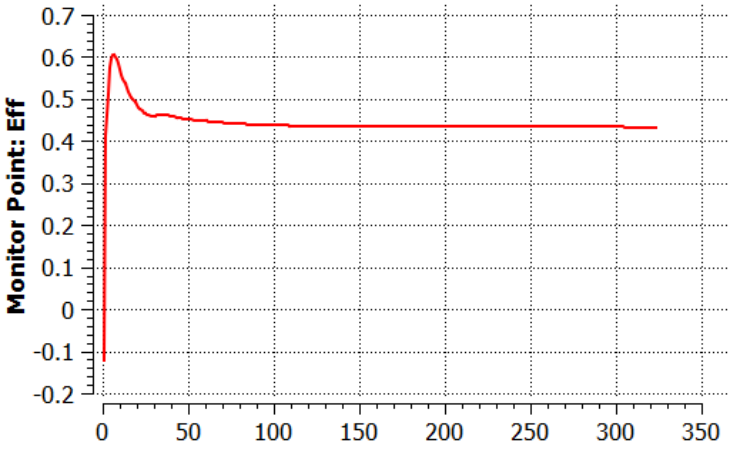

Figure 45: Efficiency of Rotor 2

The following table illustrates the optimized beta angles at the leading edge and the trailing edge of the blades, as well as the corresponding efficiency values.

Table 16: Optimum beta angle of Rotor 2

Section	r [m]	Beta_LE [Deg]	Beta_TE [Deg]	Efficiency
1	0.180	22.36	77.40	43.27%
2	0.363	44.91	83.73	
3	0.545	54.29	85.10	
4	0.728	55.35	86.10	
5	0.911	57.83	88.31	

4.2.3. Rotor 3

As shown in Figure 46, the distribution of pressure on the blade surfaces of Rotor 3 can be seen. The maximum pressure on the leading-edge pressure side decreases as one moves toward the trailing edge of the distribution. In contrast, the minimum pressure on the leading-edge suction side increases in the direction of the trailing edge.

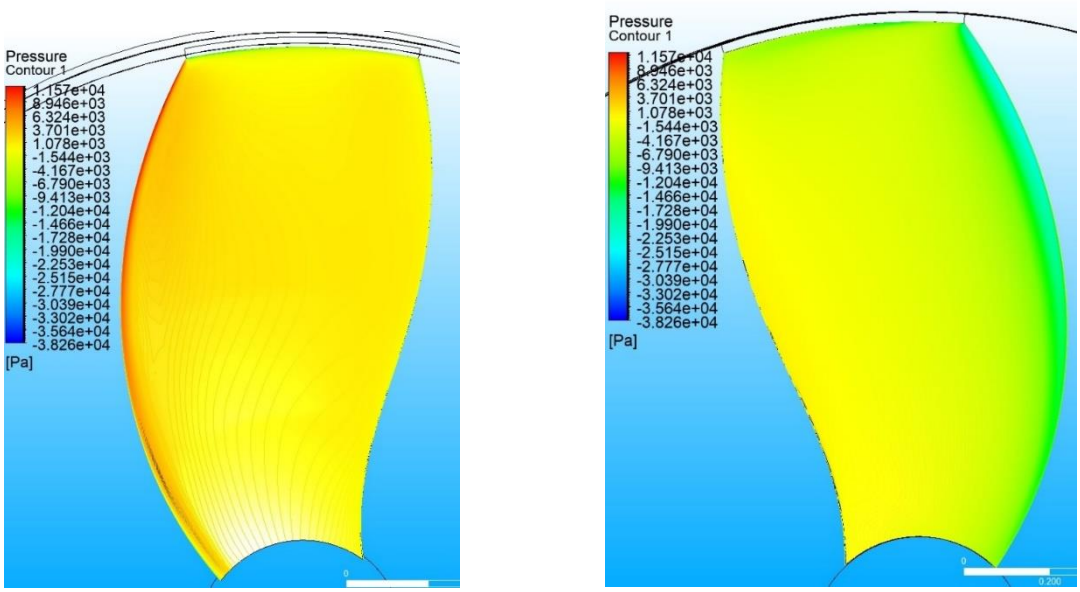

Figure 46: Pressure distribution on surface of Rotor 3

A pressure contour plot is shown in Figure 45 for a free-stream velocity of 1.6 m/s. As a result of the optimization process, the maximum pressure distribution on the pressure side leading edge was +11.570 kPa, while the minimum pressure distribution was -19.90 kPa. There is a significant difference in pressure between the leading edge and the trailing edge of the blade. The turbine achieved 43.42% efficiency of operation due to this pressure difference.

A pinnacle velocity is observed in the blade tip region of the turbine domain as shown in Figure 47. Fluid flows rapidly through the blade tip region when the velocity is high, which has a significant impact on the turbine's operation.

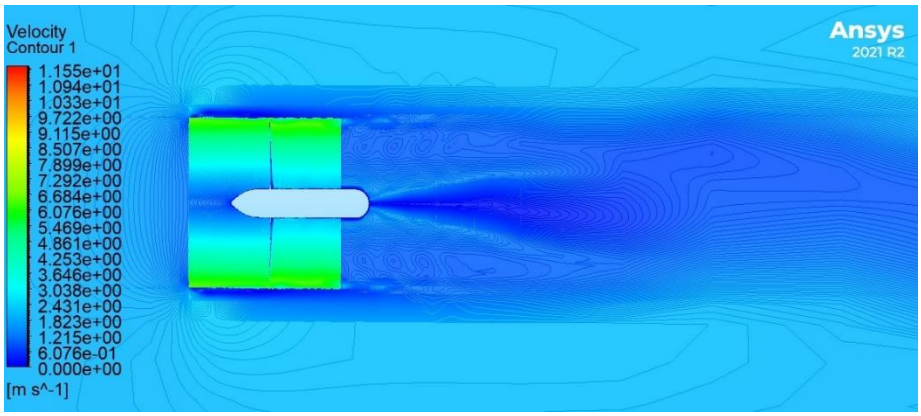

Figure 47: Velocity contour around the Rotor 3

Figures 48 illustrate the vorticity on the blade surface of Rotor 3 after optimization. Although Rotor 1 and Rotor 2 exhibited little vorticity on their surface, Rotor 3 shows a maximum level like those of Rotors 1 and 2 but with a more concentrated distribution of high values along its leading and trailing edges. This vorticity distribution may have significant implications for the flow dynamics and performance of Rotor 3 and should be considered in the optimization process

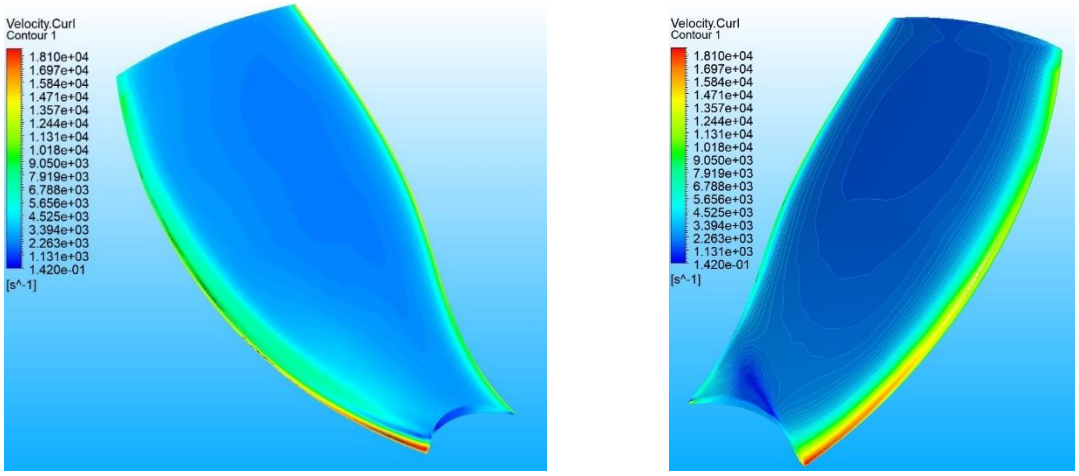

Figure 48: Vorticity on blade 3

As shown in Table 17, pressure, and viscous force, as well as pressure and viscous torque, are presented. An application of pressure force parallel to the flow direction, is used to extract the target output power from the blade surface. As shown in Table 17, the blade surface is subjected to a maximum force of 8.174 kN.

Table 17: Pressure and viscous force, pressure, and viscous torque of rotor 3

Type	X	Y	Z
Pressure Force (N)	0.469	-0.059	8156.60
Viscous Force (N)	-0.002	0.005	17.77
Total Force (N)	0.467	-0.055	8174.40
Pressure Torque (N-m)	1.612	-1.931	-1351.30
Viscous Torque (N-m)	0.0002	-0.0007	111.77
Total Torque (N-m)	1.613	-1.932	-1239.50

In Figure 49, the turbine hydraulic power of 5.8 kW is illustrated for Rotor 3 with the same available power of 13.5 kW. When generator and turbine losses are considered, an optimized output of 5.4 kW.

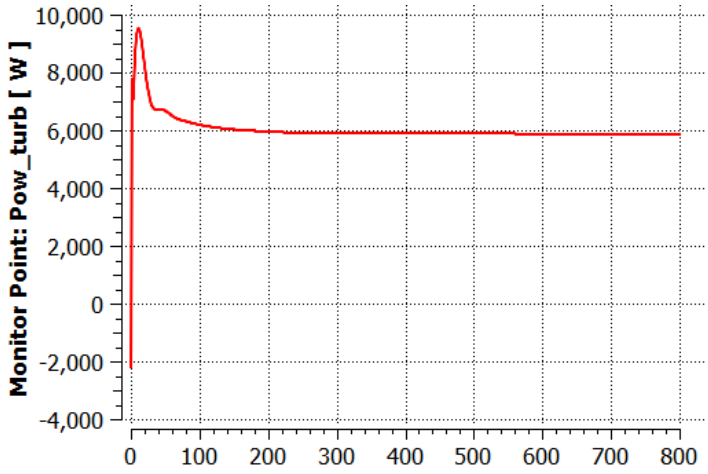

Figure 49: Power turbine of Rotor 3

According to Figure 50, Rotor 3 has an efficiency of 43.42%.

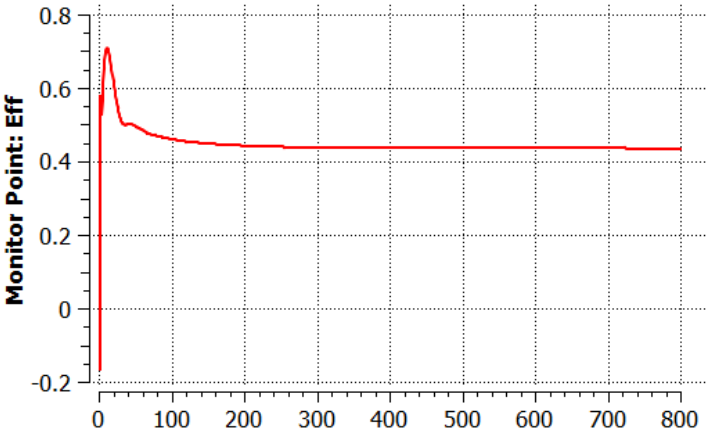

Figure 50: Efficiency of Rotor 3

Below is a table illustrating the optimized beta angles of the blades at their leading edge and their trailing edge, as well as their respective efficiency values.

Table 18 : Optimum beta angle of Rotor 3

Section	r [m]	Beta_LE [Deg]	Beta_TE [Deg]	Efficiency
1	0.250	26.37	73.80	
2	0.255	45.92	82.26	
3	0.860	54.44	86.19	43.42%
4	1.165	55.54	86.26	
5	1.469	58.19	88.67	

4.3. Efficiency

Figures 51 and 52 depict a plot of efficiency as a function of tip speed ratio (TSR) and rotations per minute (RPM). Results are presented for a range of RPM for rotors. According to the results, TSR varies between 2.5 and 5.5 and the maximum efficiency is achieved at a TSR of 4. Therefor the maximum efficiency of the rotors is reached at 172, 94, and 43 RPM. There is evidence that efficiencies above 40% can generally be achieved at speed ranges between 32 to 236 RPM.

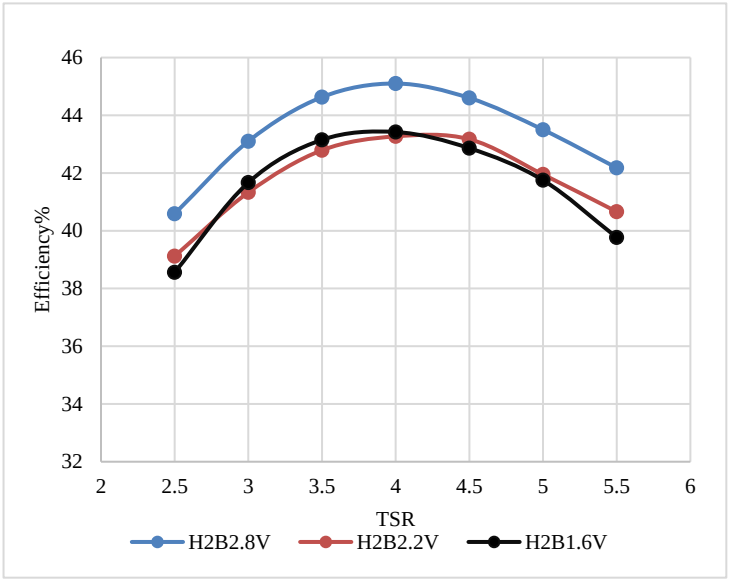

Figure 51: Pressure coefficient as function of TSR

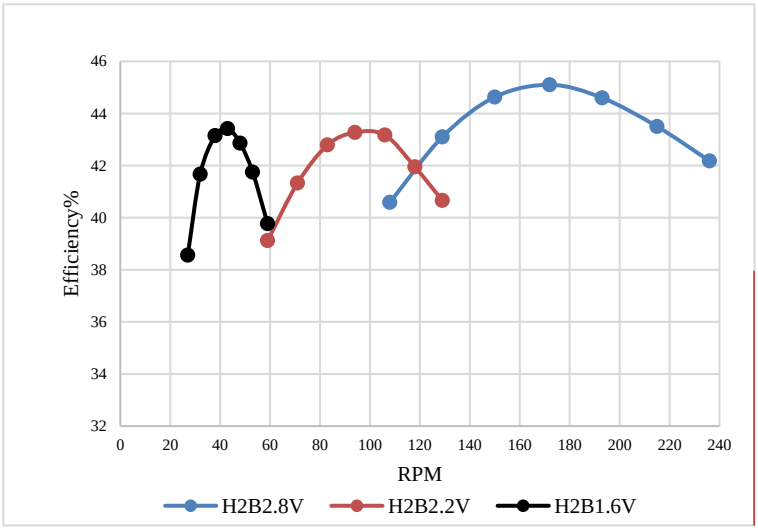

Figure 52: Pressure coefficient as a function of RPM

The most challenging aspect of this study was validating the CFD methodology using real-world data for the case studies. Furthermore, this is one of the most critical problems facing hydrokinetic turbine technology, which can be addressed through this research. The challenge was overcome by conducting a comparative analysis of simulated blades and experiment data by Stephanie Ordonez-Sanchez[57]. The maximum efficiency is shown in Figure 53 at TSR 3.6, which corresponds to 43%.

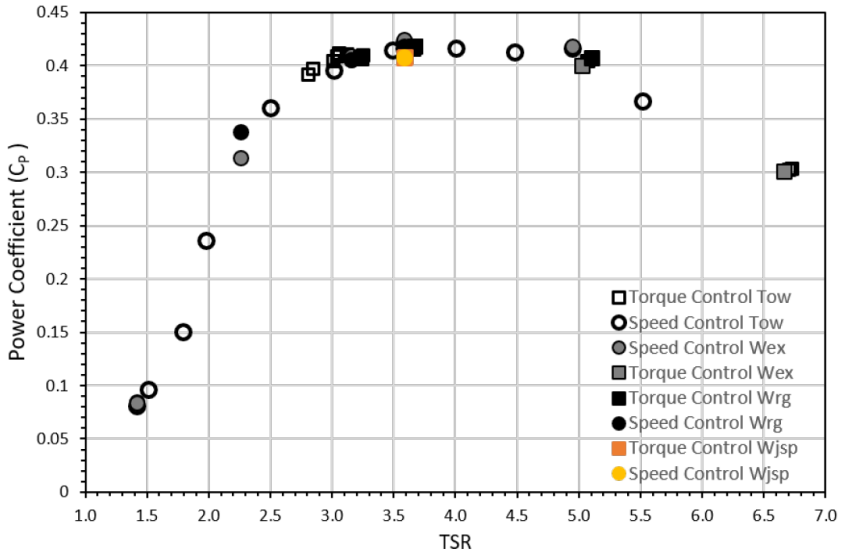

Figure 53: Experimental results extracting by Stephan Sanchez

Table 19 summarizes the dimensions and results of three rotors that were designed and optimized for the purpose of this study.

Table 19: Total rotor sizes and results

	Rotor 1	Rotor 2	Rotor 3
Number of Blades	2	2	2
Turbine Radius	0.624 m	0.896 m	1.445 m
Hub Radius	0.125 m	0.180 m	0.250 m
Free Stream Velocity	2.8 m/s	2.2 m/s	1.6 m/s
TSR	4	4	4
RPM	172	94	43
Cp	45.10	43.27	43.42

4.4. Capacity factor

As shown in Table 20, Rotor 1 capacity factor is affected by various flow stream velocity. By using only one rotor throughout the year, it is possible to achieve a maximum capacity factor of 52% based on the turbine area and pressure coefficient obtained for a simple linear velocity variation in a river. As a result of low velocity, particularly during the winter, the energy delivery decreased from 4423 to 680 kWh.

Table 20: Capacity factor of Rotor 1 using simple linear monthly velocity variation

Month	Velocity (m/s)	Radius (m)	Area (m^2)	Cp	kW	kWh
1	1.5	0.6240	1.2233	0.451	0.9	680.1
2	1.6	0.6240	1.2233	0.451	1.1	825.4
3	1.8	0.6240	1.2233	0.451	1.6	1175.2
4	2.2	0.6240	1.2233	0.451	2.9	2145.7
5	2.2	0.6240	1.2233	0.451	2.9	2145.7
6	2.8	0.6240	1.2233	0.451	6.0	4423.7
12 months						26267.6
Average kW						3.00
CF						0.52

Figure 54 shows yearly capacity factor diagram of using only one Rotor during the year.

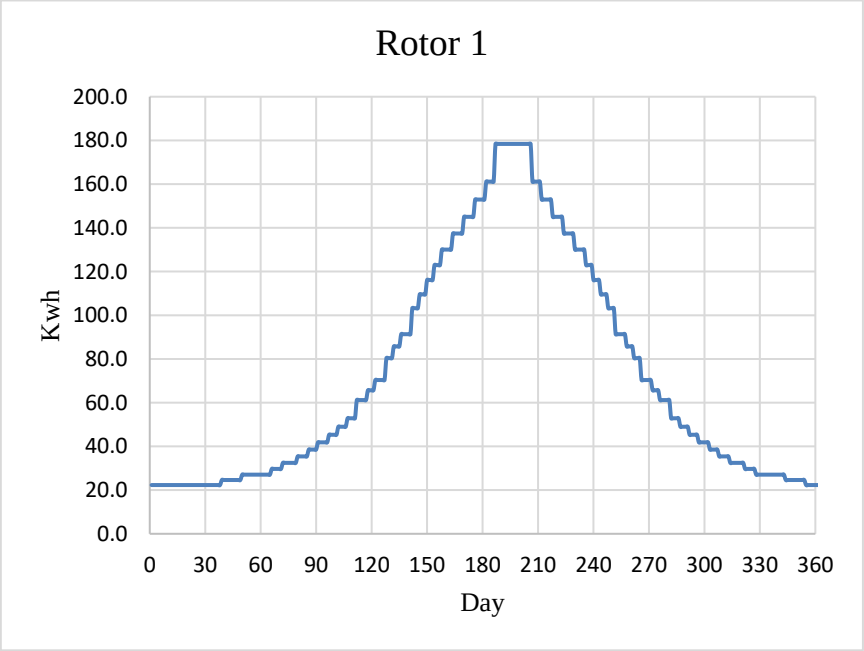

Figure 54: Yearly capacity factor by using only one Rotor

Using three interchangeable rotors during the various seasons, and changing the rotors, the capacity factor was improved from 52% to 92%. It is recommended that the rotors change depending on the velocity and the larger frontal area of rotor be used in the winter. As illustrated in Table 21 by increasing the frontal area, the capacity factor is doubled throughout the year. Through the publication of the NRCAN's yearly data river velocity, a targeted capacity factor for the entire country will be able to be exported for the current rotors.

Table 21: Simple analysis showing doubling of capacity factor by changing rotors using simple linear variation of velocity during a year

Month	Velocity (m/s)	Radius (m)	Area (m^2)	Cp	kW	kWh
1	1.5	1.4450	6.5597	0.4342	4.8	3511.2
2	1.6	1.4450	6.5597	0.4342	5.8	4261.3
3	2.0	0.8960	2.5221	0.4327	4.4	3189.0
4	2.2	0.8960	2.5221	0.4327	5.8	4244.6
5	2.6	0.6240	1.2233	0.451	4.8	3541.8
6	2.8	0.6240	1.2233	0.451	6.0	4423.7
					12 months	43445.6
					Average kW	4.96
					CF	0.92

Figure 55 illustrates yearly capacity factor diagram of using three Rotors during the year.

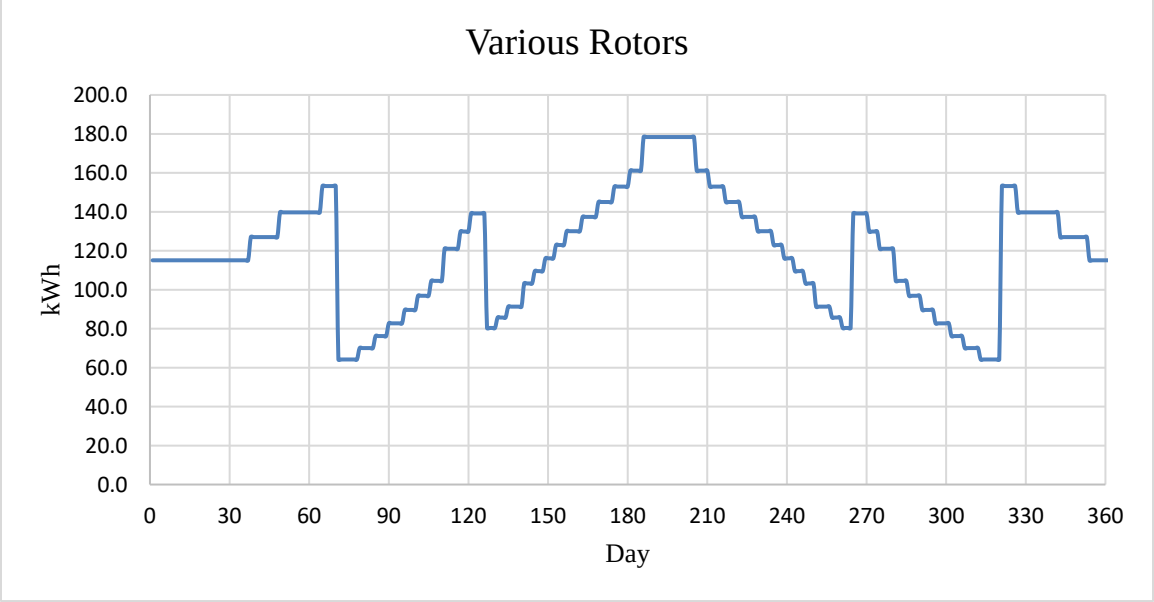

Figure 55: Yearly capacity factor by using three Rotors

4.5 Mechanical Analysis:

A detailed analysis of the blade's mechanical properties is presented in this section. Understanding the mechanical behavior of the blade is crucial for ensuring its reliability and effectiveness in each application. The maximum displacement and stress in the blade under normal steady state condition was investigated. As an imperative parameter, the load must be exactly equal to the CFD analysis results. Consequently, the load is exported from the CFX simulation results. The pressure load on the blade surface is illustrated in the following Figures.

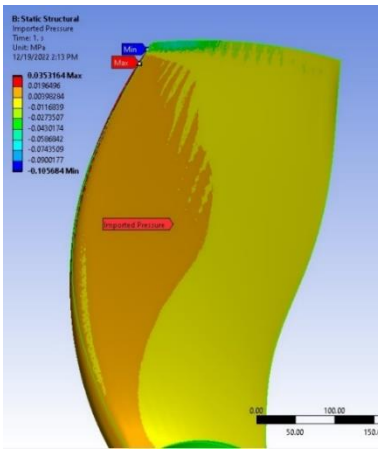

Figure 56: Load on blade 1

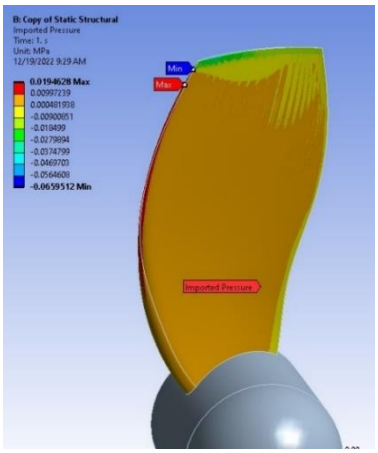

Figure 57: Load on blade 2

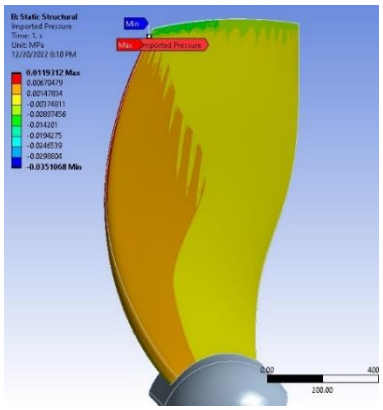

Figure 58: Load on blade 3

According to the methodology chapter, Polyether ether ketone carbon fibers and glass fibers were investigated, and their results were compared with stainless steel. The material properties of the blade, which includes tensile strength, tensile modulus, Poisson ratio and density are listed in Table 22.

The distributions of blade stress and displacement were modeled under three water velocity conditions. Figures 57 and 58 illustrate the model's simulated stress distribution and the areas subjected to maximum deformation under free stream velocity of 2.8 m/s.

Table 22: Material properties

Polyether ether ketone (PEEK) Mechanical Properties				
	Tensile strength	Tensile modulus	Density	Poisson's Modulus
	MPa	MPa	g/cc	
Glass fiber 10% - low flow	124	6206	1.37	0.38
Glass fiber 20% - low flow	152	8964	1.44	0.38
Glass fiber 30% - low flow	172	11722	1.52	0.39
Glass fiber 40% - low flow	186	15169	1.61	0.39
Carbon fiber 10% - low flow	186	11722	1.33	0.43
Carbon fiber 20% - low flow	221	19996	1.36	0.44
Carbon fiber 30% - low flow	248	25512	1.41	0.44
Carbon fiber 40% - low flow	265	34475	1.45	0.45

As shown in Figure 57, the displacement of the blade increases from the root to the tip. Up to half of the blade's length, the displacement is negligible, whereas the maximum deformation occurs at the tip.

The maximum stress is recorded in the root area near the leading edge. Figure 58 illustrates that the blade thickness can handle a maximum equivalent stress of 55.53 MPa.

A summary of the maximum deformation and equivalent stress is provided in Table 19 for Rotor 1. According to the results, PEEK-carbon fibre 40% behaves well under the specified load compared to other materials. Adding high-modulus fibres to a polymer improved the composite's tensile strength and stiffness along the fibre direction. As fibre loading raises, the tensile capacity increases, and minimum deformation was shown.

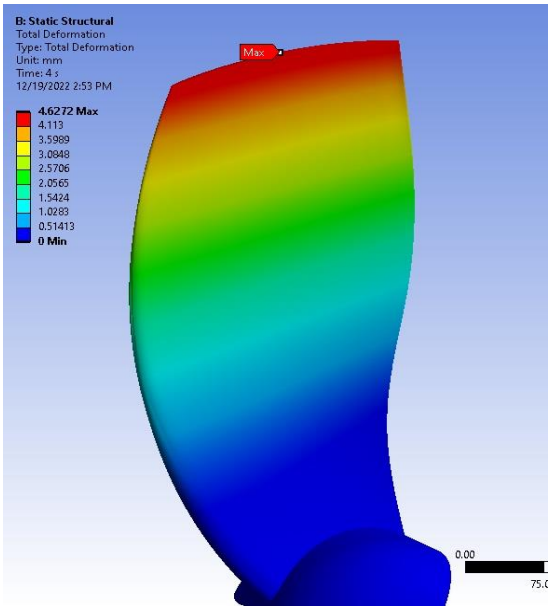

Figure 59: Maximum displacement of Rotor 1

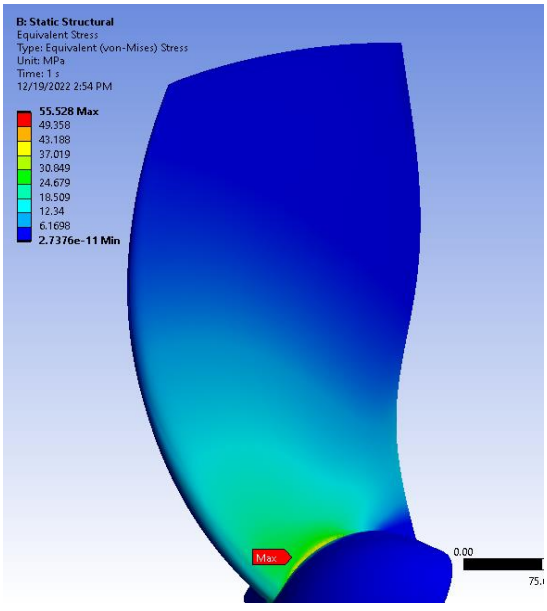

Figure 60: Maximum equivalent stress of Rotor 1

Table 23: Mechanical analysis results of Rotor 1

Material	Maximum Deformation (mm)	Maximum Equivalent Stress (MPa)
Stainless Steel	0.84	52.72
PEEK- Carbon fiber 40%	4.63	55.53
PEEK- Carbon fiber 30%	6.21	55.47
PEEK- Carbon fiber 20%	7.97	55.52
PEEK- Carbon fiber 10%	13.6	55.52
PEEK-Glass fiber 40%	14.39	56.17
PEEK- Glass fiber 30%	18.61	56.14
PEEK-Glass fiber 20%	24.32	56.10
PEEK- Glass fiber 10%	35.11	56.02

Figures 59 and 60 demonstrate the maximum displacement and stress of Rotor 2.

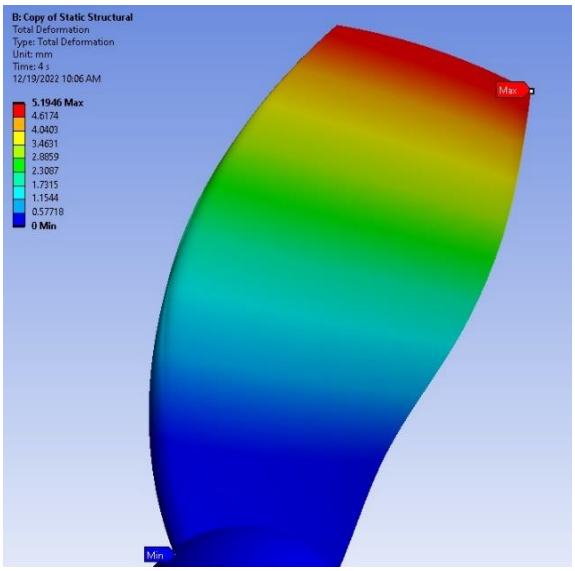

Figure 61: Maximum displacement of Rotor 2

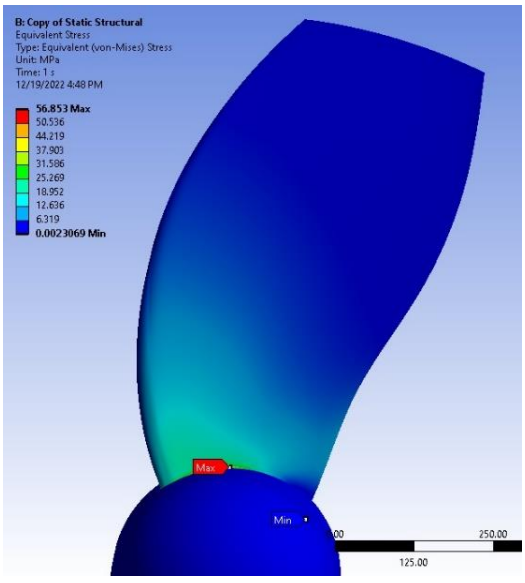

Figure 62: Maximum equivalent stress of Rotor 2

The following table presents the maximum deformation and stress of Rotor 2 under a free stream velocity of 2.2 m/s. Under the specified load, PEEK-carbon fiber 40% performed well compared to other materials.

Table 24: Mechanical results of Rotor 2

Material	Maximum Deformation (mm)	Maximum Equivalent Stress (Mpa)
Stainless Steel	0.94	55.89
PEEK- Carbon fiber 40%	5.2	56.85
PEEK- Carbon fiber 30%	6.99	56.66
PEEK- Carbon fiber 20%	8.95	56.83
PEEK- Carbon fiber 10%	15.27	56.83
PEEK-Glass fiber 40%	11.82	56.89
PEEK- Glass fiber 30%	15.28	56.88
PEEK-Glass fiber 20%	19.98	56.85
PEEK- Glass fiber 10%	28.85	56.84

The maximum displacement and stress for Rotor 3 is shown in Figures 61 and 62. As shown in Table 25, the maximum deformation and equivalent stress for Rotor 3 are summarized. Based on the results of the analysis, PEEK-carbon fiber 40% exhibits acceptable behavior under force.

According to the analysis of displacement and equivalent stress presented in this study, rotors with the material qualities suggested can be capable of withstanding equivalent stress at free stream speeds of 1.6, 2.2, and 2.8 m/s. Deformations were calculated to be 4.63, 5.20, and 5.31 mm, respectively. This was based on a displacement analysis of the rotors with the composite material parameters discussed in this work.

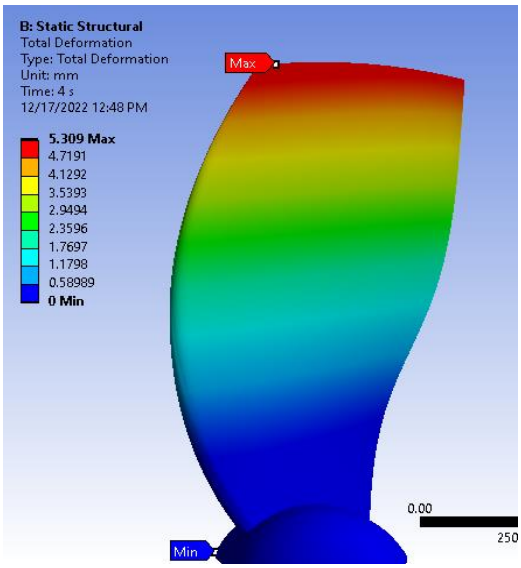

Figure 63: Maximum displacement of Rotor 3

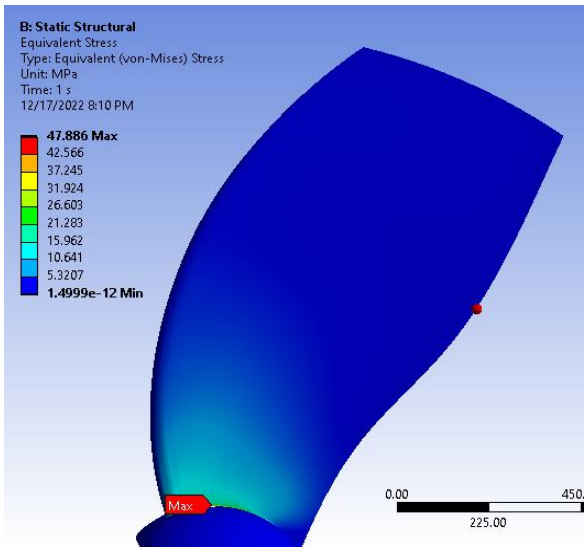

Figure 64: Maximum equivalent stress of Rotor 3

Table 25: Mechanical results of Rotor 3

Material	Maximum Deformation (mm)	Maximum Equivalent Stress (MPa)
Stainless Steel	0.97	45.9
PEEK- Carbon fiber 40%	5.31	47.89
PEEK- Carbon fiber 30%	7.15	47.89
PEEK- Carbon fiber 20%	9.15	47.89
PEEK- Carbon fiber 10%	15.61	47.89
PEEK-Glass fiber 40%	12.08	47.89
PEEK- Glass fiber 30%	15.62	47.89
PEEK-Glass fiber 20%	20.42	47.89
PEEK- Glass fiber 10%	29.49	47.89

5. Conclusion

This study aimed to offer a practical solution that can improve the capacity factor of RHKT experience variable seasonal velocities. Low flow velocities in winter can considerably impact the performance and power delivery of systems. Based on the presented method, three different sizes of interchangeable rotors were designed and optimized to produce 5 kW of output power at free-stream speeds of 1.6, 2.2, and 2.8 m/s. An excel spreadsheet was utilized to calculate initial design parameters. Several parameters, including output power, tip speed ratio, generator efficiency, turbine hydraulic and mechanical efficiency, blade number, and hub radius, were assumed and considered at the first stage.

As a starting point, the beta angle leading, and trailing edge angles were calculated with excel spreadsheet and then initial geometry was designed with BladeGen Ansys Workbench. The present study utilized CFD to analyze and investigate the fluid behavior around the blade and on the surface of rotors. This was accomplished by solving the RANS equation. By numerical approach, the blades' aerodynamic parameters were optimized to achieve a maximum efficiency of below 45%. This optimization process involved the analysis of various factors that can impact the performance of the turbine, including the flow velocity, pressure, force, and vorticity. An investigation of mesh sensitivity was conducted on the blade to determine its impact on CFD simulations.

The CFD analyses were conducted in CFX Ansys software using the SST turbulence model. Optimizing the chord line and twist angle of the hydrofoil was necessary. Several aerodynamic parameters of hydrofoils were optimized to achieve an optimum pressure difference between the pressure side and the suction side, thereby reducing significant aerodynamic losses. Blade optimization resulted in a pressure coefficient of

over 42%, compensating for the low output caused by the low free-stream velocity. At a wide range of RPMs, from 32 to 236, 5.4 and 5.6 kW of electricity was produced from the rotors with an efficiency of over 43% and 45%. In a year, the capacity factor was doubled by using three different rotor sizes.

Ansys' static structural module was used to determine the maximum displacement and equivalent stress for stainless steel, polyetheretherketone-carbon fiber, and glass fiber. PEEK-carbon fiber 40% had a minimum displacement.

Finally, the power coefficients obtained from the designed blades were compared to those obtained from the experimental results.

For future work, it is recommended that rotors be manufactured, and experimental results obtained in water tunnels or rivers be utilized to validate the simulations. In addition, structural resonance caused by turbulent water flow should be considered, as well as an equivalent static analysis. Since water acts as a dynamic load on the blade, its frequency content has an impact on its resonance mode.

References

[1] 'The Global Carbon Project'. https://www.globalcarbonproject.org/ (accessed Dec. 14, 2022).

[2] D. Gielen, F. Boshell, D. Saygin, M. D. Bazilian, N. Wagner, and R. Gorini, 'The role of renewable energy in the global energy transformation', *Energy Strategy Reviews*, vol. 24, pp. 38–50, Apr. 2019, doi: 10.1016/j.esr.2019.01.006.

[3] N. International Conference on Humanoid, Institute of Electrical and Electronics Engineers, N. International Conference on Humanoid, and HNICEM 8 2015.12.09-12 Cebu, *2015 International Conference on Humanoid, Nanotechnology, Information Technology, Communication and Control, Environment and Management (HNICEM) date: 9-12 Dec. 2015*.

[4] N. Manoj Kumar, S. S. Chopra, A. A. Chand, R. M. Elavarasan, and G. M. Shafiullah, 'Hybrid renewable energy microgrid for a residential community: A techno-economic and environmental perspective in the context of the SDG7', *Sustainability (Switzerland)*, vol. 12, no. 10, May 2020, doi: 10.3390/SU12103944.

[5] M. Arriaga, E. Nasr, and H. Rutherford, 'Renewable Energy Microgrids in Northern Remote Communities', *IEEE Potentials*, vol. 36, no. 5, pp. 22–29, Sep. 2017, doi: 10.1109/MPOT.2017.2702798.

[6] M. Arriaga, E. Nasr, and H. Rutherford, 'Renewable Energy Microgrids in Northern Remote Communities', *IEEE Potentials*, vol. 36, no. 5, pp. 22–29, Sep. 2017, doi: 10.1109/MPOT.2017.2702798.

[7] S. P. Bihari *et al.*, 'A Comprehensive Review of Microgrid Control Mechanism and Impact Assessment for Hybrid Renewable Energy Integration', *IEEE Access*, vol. 9. Institute of Electrical and Electronics Engineers Inc., pp. 88942–88958, 2021. doi: 10.1109/ACCESS.2021.3090266.

[8] O. Hafez and K. Bhattacharya, 'Optimal planning and design of a renewable energy based supply system for microgrids', *Renew Energy*, vol. 45, pp. 7–15, 2012, doi: 10.1016/j.renene.2012.01.087.

[9] 'Natural Resources Canada', Mar. 12, 2014.

[10] Z. U. Khan, Z. Ali, and E. Uddin, 'Performance enhancement of vertical axis hydrokinetic turbine using novel blade profile', *Renew Energy*, vol. 188, pp. 801–818, Apr. 2022, doi: 10.1016/j.renene.2022.02.050.

[11] S. Subhra Mukherji, N. Kolekar, A. Banerjee, and R. Mishra, 'Numerical investigation and evaluation of optimum hydrodynamic performance of a horizontal axis hydrokinetic turbine', *Journal of Renewable and Sustainable Energy*, vol. 3, no. 6, Nov. 2011, doi: 10.1063/1.3662100.

[12] A. Muratoglu and M. I. Yuce, 'Performance Analysis of Hydrokinetic Turbine Blade Sections', 2015.

[13] A. Betz, *Introduction to the Theory of Flow Machines*, [1st English ed.]. Oxford; New York, Pergamon Press, 1966.

[14] J. Aguilar, A. Rubio-Clemente, L. Velasquez, and E. Chica, 'Design and optimization of a multi-element hydrofoil for a horizontal-axis hydrokinetic turbine', *Energies (Basel)*, vol. 12, no. 24, Dec. 2019, doi: 10.3390/en12244679.

[15] A. M. Plagge, L. Jestings, and B. P. Epps, 'NEXT-GENERATION HYDROKINETIC POWER TAKE-OFF VIA A NOVEL VARIABLE-STROKE HYDRAULIC SYSTEM', 2014. [Online]. Available: http://www.asme.org/about-asme/terms-of-use

[16] D. Ramírez, A. Rubio-Clemente, and E. Chica, 'Design and numerical analysis of an efficient H-Darrieus vertical-axis hydrokinetic turbine', *Journal of Mechanical Engineering and Sciences*, vol. 13, no. 4, pp. 6036–6058, 2019, doi: 10.15282/jmes.13.4.2019.21.0477.

[17] Y. W. Chong, W. Ismail, K. Ko, and C. Y. Lee, 'Energy Harvesting for Wearable Devices: A Review', *IEEE Sens J*, vol. 19, no. 20, pp. 9047–9062, Oct. 2019, doi: 10.1109/JSEN.2019.2925638.

[18] H. A. Zakaria and C. M. Loon, 'The Application of Piezoelectric Sensor as Energy Harvester from Small-scale Hydropower', in *E3S Web of Conferences*, Nov. 2018, vol. 65. doi: 10.1051/e3sconf/20186505024.

[19] ~ 4 Elsevier, L. Gagnon, and J. F. van de Vate, 'Greenhouse gas emissions from hydropower The state of research in 1996', 1997.

[20] M. S. Güney and K. Kaygusuz, 'Hydrokinetic energy conversion systems: A

technology status review', *Renewable and Sustainable Energy Reviews*, vol. 14, no. 9. Elsevier Ltd, 2010. doi: 10.1016/j.rser.2010.06.016.

[21] P. Döll, K. Fiedler, and J. Zhang, 'Hydrology and Earth System Sciences Global-scale analysis of river flow alterations due to water withdrawals and reservoirs', 2009. [Online]. Available: www.hydrol-earth-syst-sci.net/13/2413/2009/

[22] A. Briones Hidrovo, J. Uche, and A. Martínez-Gracia, 'Accounting for GHG net reservoir emissions of hydropower in Ecuador', *Renew Energy*, vol. 112, pp. 209–221, 2017, doi: 10.1016/j.renene.2017.05.047.

[23] 'EnviroGen 250 Tidal Series', Feb. 10, 2023.

[24] M. Sood and S. K. Singal, 'Development of hydrokinetic energy technology: A review', *International Journal of Energy Research*, vol. 43, no. 11. John Wiley and Sons Ltd, pp. 5552–5571, Sep. 01, 2019. doi: 10.1002/er.4529.

[25] 'The EnviroGen Series Turbine', Feb. 10, 2023.

[26] C. M. Puertas-Frías, C. S. Willson, and P. A. García-Salaberri, 'Design and economic analysis of a hydrokinetic turbine for household applications', *Renew Energy*, vol. 199, pp. 587–598, Nov. 2022, doi: 10.1016/j.renene.2022.08.155.

[27] C. M. Niebuhr, M. van Dijk, V. S. Neary, and J. N. Bhagwan, 'A review of hydrokinetic turbines and enhancement techniques for canal installations: Technology, applicability and potential', *Renewable and Sustainable Energy Reviews*, vol. 113. Elsevier Ltd, Oct. 01, 2019. doi: 10.1016/j.rser.2019.06.047.

[28] P. K. Yadav, A. Kumar, and S. Jaiswal, 'A critical review of technologies for harnessing the power from flowing water using a hydrokinetic turbine to fulfill the energy need', *Energy Reports*, vol. 9. Elsevier Ltd, pp. 2102–2117, Dec. 01, 2023. doi: 10.1016/j.egyr.2023.01.033.

[29] A. B. Mohamed, C. Bear, M. Bear, and A. Korobenko, 'Performance analysis of two vertical-axis hydrokinetic turbines using variational multiscale method', *Comput Fluids*, vol. 200, Mar. 2020, doi: 10.1016/j.compfluid.2020.104432.

[30] S. Mathew and G.S. Philip, 'Comprehensive Renewable Energy', Second Edition., Trevor M. Letcher, Ed. 2022.

[31] F. Mühle, M. S. Adaramola, and L. Sretran, 'The effect of the number of blades on wind turbine wake - A comparison between 2-and 3-bladed rotors', in *Journal of Physics: Conference Series*, Oct. 2016, vol. 753, no. 3. doi: 10.1088/1742-6596/753/3/032017.

[32] M. J. Khan, G. Bhuyan, M. T. Iqbal, and J. E. Quaicoe, 'Hydrokinetic energy conversion systems and assessment of horizontal and vertical axis turbines for river and tidal applications: A technology status review', *Applied Energy*, vol. 86, no. 10. Elsevier Ltd, pp. 1823–1835, 2009. doi: 10.1016/j.apenergy.2009.02.017.

[33] P. Mycek, B. Gaurier, G. Germain, G. Pinon, and E. Rivoalen, 'Numerical and experimental study of the interaction between two marine current turbines', *International Journal of Marine Energy*, vol. 1, pp. 70–83, 2013, doi: 10.1016/j.ijome.2013.05.007.

[34] M. Abdou and M. Kasem, 'Aerodynamic, Structural and Aeroelastic Design of Wind Turbine Blades', 200AD. [Online]. Available: www.intechopen.com

[35] H. Snel, 'Review of the present status of rotor aerodynamics'.

[36] P. J. Moriarty and A. C. Hansen, 'AeroDyn Theory Manual', 2005. [Online]. Available: http://www.osti.gov/bridge

[37] J. M. Jonkman, 'Modeling of the UAE Wind Turbine for Refinement of FAST_AD', 2003. [Online]. Available: http://www.osti.gov/bridge

[38] J. Tangler, J. D. Kocurek, and J. L. Tangler, 'Wind Turbine Post-Stall Airfoil Performance Characteristics Guidelines for Blade-Element Momentum Methods Preprint Wind Turbine Post-Stall Airfoil Performance Characteristics Guidelines for Blade-Element Momentum Methods', 2004. [Online]. Available: http://www.osti.gov/bridgeonlineordering:http://www.ntis.gov/ordering.htm

[39] J. F. Manwell, J. G. McGowan, and A. L. Rogers, *Wind energy explained : theory, design and application*. Wiley, 2009.

[40] M. J. Jahromi, A. I. Maswood, and K. J. Tseng, 'Long term prediction of tidal currents', *IEEE Syst J*, vol. 5, no. 2, pp. 146–155, Jun. 2011, doi: 10.1109/JSYST.2010.2090401.

[41] Institute of Electrical and Electronics Engineers. and Marine Technology Society., *Oceans '08 MTS/IEEE Quebec : Oceans, Poles & Climate: Technological Challenges : Sept. 15-18, 2008, Quebec City Convention Centre, Quebec City, Canada.* IEEE, 2008.

[42] S. Ordonez-Sanchez *et al.*, 'Analysis of a horizontal-axis tidal turbine performance in the presence of regular and irregular waves using two control strategies', *Energies (Basel)*, vol. 12, no. 3, Jan. 2019, doi: 10.3390/en12030367.

[43] E. Chica and A. Rubio-Clemente, 'Design of Zero Head Turbines for Power Generation', in *Renewable Hydropower Technologies*, InTech, 2017. doi: 10.5772/66907.

[44] E. B. Fundamentals and R. Applications, 'Wind Turbine Aerodynamics and Vorticity-Based Methods'. [Online]. Available: http://www.springer.com/series/11859

[45] J. Rom, *High Angle of Attack Aerodynamics*. New York, NY: Springer New York, 1992. doi: 10.1007/978-1-4612-2824-0.

[46] 'Interpretation of Bernoulli's equation'.

[47] David C. Wilcox, 'Formulation of the k-omega Turbulence Model Revisited', Nov. 2008.

[48] B. Bastl, M. Brandner, J. Egermaier, K. Michálková, and E. Turnerová, 'Isogeometric analysis for turbulent flow', *Math Comput Simul*, vol. 145, pp. 3–17, Mar. 2018, doi: 10.1016/j.matcom.2016.05.010.

[49] S. Suhas Kulkarni, C. Chapman, H. Shah, E. A. Pärn, D. J. Edwards, and S. S. Kulkarni, 'Design Study of Horizontal Axis Tidal Turbine Blade', 2017.

[50] S. S. Kulkarni, C. Chapman, and H. Shah, 'Computational Fluid Dynamics (CFD) Mesh Independency Study of A Straight Blade Horizontal Axis Tidal Turbine', doi: 10.20944/preprints201608.0008.v1.

[51] T. P. Chang, F. J. Liu, H. H. Ko, S. P. Cheng, L. C. Sun, and S. C. Kuo, 'Comparative analysis on power curve models of wind turbine generator in estimating capacity factor', *Energy*, vol. 73, pp. 88–95, Aug. 2014, doi: 10.1016/j.energy.2014.05.091.

[52] J. S. Chou, C. K. Chiu, I. K. Huang, and K. N. Chi, 'Failure analysis of wind turbine blade under critical wind loads', *Eng Fail Anal*, vol. 27, pp. 99–118, Jan. 2013, doi: 10.1016/j.engfailanal.2012.08.002.

[53] K. Kalkanis, C. S. Psomopoulos, S. Kaminaris, G. Ioannidis, and P. Pachos, 'Wind turbine blade composite materials - End of life treatment methods', in *Energy Procedia*, 2019, vol. 157, pp. 1136–1143. doi: 10.1016/j.egypro.2018.11.281.

[54] M. J. Pawar, A. Patnaik, and R. Nagar, 'Mechanical and thermo-mechanical analysis based numerical simulation of granite powder filled polymer composites for wind turbine blade', *Fibers and Polymers*, vol. 17, no. 7, pp. 1078–1089, Jul. 2016, doi: 10.1007/s12221-016-5843-y.

[55] M. J. Pawar, A. Patnaik, and R. Nagar, 'Mechanical and thermo-mechanical analysis based numerical simulation of granite powder filled polymer composites for wind turbine blade', *Fibers and Polymers*, vol. 17, no. 7, pp. 1078–1089, Jul. 2016, doi: 10.1007/s12221-016-5843-y.

[56] S. Sarkar and P. R. Voke, 'Large-eddy simulation of unsteady surface pressure over a low-pressure turbine blade due to interactions of passing wakes and inflexional boundary layer', *J Turbomach*, vol. 128, no. 2, pp. 221–231, Apr. 2006, doi: 10.1115/1.2137741.

[57] S. Ordonez-Sanchez *et al.*, 'Analysis of a horizontal-axis tidal turbine performance in the presence of regular and irregular waves using two control strategies', *Energies (Basel)*, vol. 12, no. 3, Jan. 2019, doi: 10.3390/en12030367.